



HAL
open science

Comprehension of the Route for the Synthesis of Co/Fe LDHs via the Method of Coprecipitation with Varying pH

Chérif Morcos, Alain Seron, Nicolas Maubec, Ioannis Ignatiadis, Stéphanie Betelu

► **To cite this version:**

Chérif Morcos, Alain Seron, Nicolas Maubec, Ioannis Ignatiadis, Stéphanie Betelu. Comprehension of the Route for the Synthesis of Co/Fe LDHs via the Method of Coprecipitation with Varying pH. *Nanomaterials*, 2022, 12 (9), pp.1570. 10.3390/nano12091570 . hal-03684256

HAL Id: hal-03684256

<https://brgm.hal.science/hal-03684256>

Submitted on 1 Jun 2022

HAL is a multi-disciplinary open access archive for the deposit and dissemination of scientific research documents, whether they are published or not. The documents may come from teaching and research institutions in France or abroad, or from public or private research centers.

L'archive ouverte pluridisciplinaire **HAL**, est destinée au dépôt et à la diffusion de documents scientifiques de niveau recherche, publiés ou non, émanant des établissements d'enseignement et de recherche français ou étrangers, des laboratoires publics ou privés.

Article

Comprehension of the Route for the Synthesis of Co/Fe LDHs via the Method of Coprecipitation with Varying pH

Chérif Morcos^{1,2}, Alain Seron^{1,*}, Nicolas Maubec¹, Ioannis Ignatiadis¹ and Stéphanie Betelu^{1,*}

¹ BRGM, French Geological Survey, 3 Avenue Claude Guillemin, CEDEX 02, 45060 Orleans, France; c.morcos@brgm.fr (C.M.); n.maubec@brgm.fr (N.M.); i.ignatiadis@brgm.fr (I.I.)

² LGC, Chemical Engineering Laboratory, University of Toulouse III, 118 Route de Narbonne, CEDEX 09, 31062 Toulouse, France

* Correspondence: a.seron@brgm.fr (A.S.); s.betelu@brgm.fr (S.B.)

Abstract: Co/Fe-based layered double hydroxides (LDHs) are among the most promising materials for electrochemical applications, particularly in the development of energy storage devices, such as electrochemical capacitors. They have also been demonstrated to function as energy conversion catalysts in photoelectrochemical applications for CO₂ conversion into valuable chemicals. Understanding the formation mechanisms of such compounds is therefore of prime interest for further controlling the chemical composition, structure, morphology, and/or reactivity of synthesized materials. In this study, a combination of X-ray diffraction, vibrational and absorption spectroscopies, as well as physical and chemical analyses were used to provide deep insight into the coprecipitation formation mechanisms of Co/Fe-based LDHs under high supersaturation conditions. This procedure consists of adding an alkaline aqueous solution (2.80 M NaOH and 0.78 M Na₂CO₃) into a cationic solution (0.15 M Co^{II} and 0.05 M Fe^{III}) and varying the pH until the desired pH value is reached. Beginning at pH 2, pH increases induce precipitation of Fe^{III} as ferrihydrite, which is the pristine reactional intermediate. From pH > 2, Co^{II} sorption on ferrihydrite promotes a redox reaction between Fe^{III} of ferrihydrite and the sorbed Co^{II}. The crystallinity of the poorly crystallized ferrihydrite progressively decreases with increasing pH. The combination of such a phenomenon with the hydrolysis of both the sorbed Co^{III} and free Co^{II} generates pristine hydroxylated Fe^{II}/Co^{III} LDHs at pH 7. Above pH 7, free Co^{II} hydrolysis proceeds, which is responsible for the local dissolution of pristine LDHs and their reprecipitation and then 3D organization into Co^{II}₄Fe^{II}₂Co^{III}₂ LDHs. The progressive incorporation of Co^{II} into the LDH structure is accountable for two phenomena: decreased coulombic attraction between the positive surface-charge sites and the interlayer anions and, concomitantly, the relative redox potential evolution of the redox species, such as when Fe^{II} is re-oxidized to Fe^{III}, while Co^{III} is re-reduced to Co^{II}, returning to a Co^{II}₆Fe^{III}₂ LDH. The nature of the interlamellar species (OH⁻, HCO₃⁻, CO₃²⁻ and NO₃⁻) depends on their mobility and the speciation of anions in response to changing pH.

Keywords: Co/Fe LDH formation mechanism; reaction intermediates; ferrihydrite; Co^{II} sorption; Co/Fe redox reactions



Citation: Morcos, C.; Seron, A.; Maubec, N.; Ignatiadis, I.; Betelu, S. Comprehension of the Route for the Synthesis of Co/Fe LDHs via the Method of Coprecipitation with Varying pH. *Nanomaterials* **2022**, *12*, 1570. <https://doi.org/10.3390/nano12091570>

Academic Editors: John Vakros, Evroula Hapeshi, Catia Cannilla and Giuseppe Bonura

Received: 3 March 2022

Accepted: 25 April 2022

Published: 6 May 2022

Publisher's Note: MDPI stays neutral with regard to jurisdictional claims in published maps and institutional affiliations.



Copyright: © 2022 by the authors. Licensee MDPI, Basel, Switzerland. This article is an open access article distributed under the terms and conditions of the Creative Commons Attribution (CC BY) license (<https://creativecommons.org/licenses/by/4.0/>).

1. Introduction

Layered double hydroxides (LDHs) are a group of minerals consisting of stacked brucite-like layers. They can be represented by the general formula [M_{1-x}^{II}M_x^{III}(OH)₂](Aⁿ⁻)_{x/n}·mH₂O, where M^{II} (e.g., Mg²⁺, Co²⁺, ...) and M^{III} (e.g., Fe³⁺, Al³⁺, ...) are the divalent and trivalent cations, respectively; *x* is the molar ratio M^{III}/(M^{II} + M^{III}) [1–5]. According to the abovementioned formula, *m* is the number of water molecules intercalated in the interlamellar space of the LDH structure. The positive charge, due to the presence of the trivalent cations, is balanced by exchangeable anions Aⁿ⁻ that are located in the interlamellar space and whose width depends on, among other things, the size and nature

of the intercalated anions (CO_3^{2-} , Cl^- , $\text{NO}_3^- \dots$). Several synthesis routes, such as coprecipitation, the urea hydrolysis method and the sol-gel method [5,6], are described in the scientific literature for synthesizing LDHs of a broad range of formulations [7] and particle sizes ($1 \text{ nm} < d < 10 \text{ }\mu\text{m}$) with various morphologies [8], leading to a large spectrum of specific surface area values up to $\sim 100 \text{ m}^2 \cdot \text{g}^{-1}$ [9–11]. The synthesis route is also responsible for a diversity of intercalated anions (CO_3^{2-} , Cl^- , HCO_3^- , $\text{NO}_3^- \dots$) with tunable affinity depending on the anions in dynamic equilibrium with the media, even if CO_3^{2-} tends to have one of the highest affinities for most LDHs [12]. LDHs are well-known for their anionic exchange capacity (AEC) in interlamellar space [13–15], which varies between 2 and 5 $\text{meq} \cdot \text{g}^{-1}$ [16,17]. For these reasons, LDHs have attracted significant interest for industrial and environmental applications [7,18–23]. Moreover, LDHs were recently demonstrated as being among the most promising materials for the photoelectrochemical reduction of CO_2 , due to their capacity to facilitate the elaboration of sophisticated catalysts, among other things [24]. Coprecipitation is the most common synthesis route [4,25,26]. Two methods of coprecipitation are used, involving (i) high supersaturation and (ii) low supersaturation [27]. The low supersaturation method consists of adding a solution containing a mixture of M^{II} and M^{III} cations at the desired molar ratio as precursor salts to an alkaline aqueous solution containing the desired anions and maintaining the pH at the selected value. The high supersaturation method consists of adding both a titrant into the cationic solution and the alkaline aqueous solution containing the anion to be intercalated, and the pH is varied until the desired value is reached. This last method promotes nucleation at the expense of particle growth and consequently produces crystallites of small sizes [28,29].

Many studies have been conducted in order to understand the coprecipitation processes and mechanisms leading to LDH formation. For the synthesis of LDHs containing Mg/Al, Mg/Fe, Co/Al and Cr/Zn, Bocclair et al. [30,31] found that two buffered pH ranges (plateaus) are observed during the titration of the solution containing both divalent and trivalent cations using an alkaline solution. Hydroxyl anions cause the trivalent cation to precipitate as low-soluble hydroxide or oxyhydroxide during the first plateau. During the second plateau, hydroxyl anions are responsible for the coprecipitation of M^{II} and M^{III} cations, resulting in LDH formation. The pH value range of this second precipitation event is located between those of M^{II} and M^{III} precipitation.

For Mg/Al and Ni/Fe LDHs, Radha et al. [32] proposed a mechanism consisting of the precipitation of a trivalent cation into an amorphous phase that dissolves before the coprecipitation of divalent and trivalent cations for the obtainment of LDHs. For Ni/Fe LDHs, Grégoire et al. [33] identified the precipitation of akaganeite ($\beta\text{-Fe}^{\text{III}}\text{O}(\text{OH},\text{Cl})$), occurring at the beginning of the titration, as a precursor for the first pH plateau. The presence of Ni^{2+} in the medium prevents the transformation of akaganeite to goethite. Indeed, the progressive pH increase leads to akaganeite being negatively charged. In such conditions, $[\text{Ni}(\text{H}_2\text{O})_6]^{2+}$ reacts with the hydroxyl surface of the akaganeite to form a cationic complex $[\text{Ni}(\text{OH})(\text{H}_2\text{O})_5]^+$. The hydroxylation of this cationic complex continues until the appearance of a neutral complex $[\text{Ni}(\text{OH})_2(\text{H}_2\text{O})_4]$, which forms a lamellar $\alpha\text{-}[\text{Ni}(\text{OH})_{1-\delta}(\text{H}_2\text{O})_\delta]^+$ phase via an olation reaction [34]. This positive phase may be adsorbed on the oxygen atoms of the hydroxyl groups of the negative ferric phase. This adsorption may assist the diffusion of iron from the akaganeite to the Ni hydroxide phase, thus generating the LDH layers. After the formation of the Ni/Fe LDHs, two hydroxide phases, $\beta\text{-Fe}^{\text{III}}\text{O}(\text{OH},\text{Cl})$ and $\alpha\text{-}[\text{Ni}(\text{OH})_{1-\delta}(\text{H}_2\text{O})_\delta]^+$, were reported [13] using Raman spectroscopy, even after a hydrothermal treatment.

Since the 2010s, Co/Fe LDHs have been extensively investigated as efficient, reliable and robust catalysts or supercapacitors [35–43]. The presence of the $\text{Co}^{\text{III}}/\text{Co}^{\text{II}}$ pair in LDHs significantly improves the conductivity and reversibility of electron transfer [44–46]. Integrated into the formulation of LDHs, Fe^{III} promotes electronic transfer via the hopping mechanism, due to its electron-acceptor nature [47,48]. The use of Co-based LDHs as electrophotocatalyzers was also demonstrated in the conversion of atmospheric CO_2 into

CH₄ [49]. Consequently, compounds based on cobalt and iron represent a major stack in the development of advanced technologies. Understanding the formation mechanisms of such compounds is thus of prime interest.

To the best of our knowledge, this study is the first to investigate the formation mechanisms of Co/Fe LDHs by coprecipitation via the high supersaturation method at 35 °C [7]. Both pH and conductivity were monitored throughout the titration for investigation of the physical and chemical parameters of the solution, while atomic absorption spectroscopy was used to determine the residual concentrations of the M^{II} and M^{III} cations.

The powder X-ray diffractometry (PXRD) characterization of the solids obtained at different pH levels allowed us to determine their structure, crystallinity and purity. The nature of the interlamellar anions was studied by FTIR (Fourier transform infrared) spectroscopy.

2. Experimental Section

2.1. Chemicals

All chemicals (>99.8% purity) used for the Co/Fe LDH synthesis were supplied by Merck-Sigma-Aldrich (Merck KGaA, Darmstadt, Germany): Co(NO₃)₂·6H₂O, Fe(NO₃)₃·9H₂O, Na₂CO₃ and NaOH. KBr (>99% purity) used for FTIR measurements was supplied by Merck-Sigma-Aldrich. An Fe standard solution of 1000 ppm (Fe(NO₃)₃ in 0.5 M HNO₃, Certipur[®], Burlington, MA, US), ammonium acetate (ACS reagent, ≥97%), acetic acid (ACS reagent, ≥99.7%), hydroxylamine hydrochloride (ReagentPlus[®], Burlington, MA, US, 99%) and 1,10-phenanthroline hydrochlorate (ReagentPlus[®], 99%) were used for UV–visible spectrophotometric measurements.

2.2. Coprecipitation Methodology, Solids Purification and Aging

The coprecipitation of trivalent Fe and divalent Co cations was investigated via the continuous injection of an alkaline titrant into a cationic aqueous mixture in the pH range of 2 to 11 until reaching the desired pH end value. Nine titration experiments, corresponding to nine different pH end values, were performed using 100 mL solutions of Co^{II} (0.15 M) and Fe^{III} (0.05 M). The initial pH value of the Co^{II}/Fe^{III} solution was 1.8. The titrant used was a solution of NaOH (2.80 M) and Na₂CO₃ (0.78 M).

The titrant was added accurately at $3.9 \pm 0.1 \mu\text{L}\cdot\text{s}^{-1}$ using an automatic titrator (Metrohm model Titrando; technology Dosino, Herisau, Switzerland) under vigorous stirring (500 rpm). Titrations were conducted under atmospheric air and pressure in a thermoregulated 150 mL cylindrical Pyrex double-walled water-jacketed reactor at 35 ± 0.2 °C (DC10-P5/U thermostat bath, Haake, Vreden, Germany). During titrations, pH values ($\pm 0.3\%$) of the titrated solutions were recorded as a function of the injected volume of titrant solution; measurements of conductivity and temperature were also continuously recorded with a data-acquisition system (Keithley Instruments, model 2700, Cleveland, OH, USA) controlled by a computer equipped with KickStart 2.5.0 software from Keithley Instruments.

After the pH reached the desired end value, the obtained slurries were centrifuged at 4000 rpm for 15 min to eliminate the supernatants containing the remaining reagents. Then, the resulting slurry underwent 5 dialysis steps of 24 h each in milliQ water (18 MΩ·cm at 25 °C) to remove residual reagent. To allow for the structural characterization of the solids, powders were obtained by freeze drying the slurry at -80 °C and 0.02 mbar using a Christ Alpha 2–4 LSCPlus freeze dryer (Martin Christ Gefrier Trocknungsanlagen GmbH, Osterode am Harz, Germany).

For optimal use in the intended applications, LDH particles should be stored as slurries to facilitate handling and hydrodynamic transport and avoid single particle agglomeration. Consequently, synthesized solids were stocked as particles dispersed into fresh milliQ water at room temperature in sealed polyethylene flasks. The influence of aging (700 days) was investigated in such specific conditions.

2.3. Physical and Chemical Characterization of the Solids

Obtained solids were ground, using an agate pestle and mortar. In order to determine the nature of the crystalline phases, PXRD analyses were recorded from 5 to 75° in 2θ by using a Bruker D8 Advance diffractometer (Palaiseau, France) using a copper anticathode ($\lambda K\alpha \approx 0.1542$ nm). The lattice parameters were calculated using the following Equations (1)–(3):

$$\frac{1}{d_{hkl}^2} = \frac{h^2}{a^2} + \frac{k^2}{b^2} + \frac{l^2}{c^2} \quad (1)$$

for orthorhombic crystalline systems,

$$\frac{1}{d_{hkl}^2} = \frac{h^2 + k^2}{a^2} + \frac{l^2}{c^2} \quad (2)$$

for trigonal crystalline systems, and

$$\frac{1}{d_{hkl}^2} = \frac{4(h^2 + hk + k^2)}{3a^2} + \frac{l^2}{c^2} \quad (3)$$

for hexagonal crystalline systems.

The average LDH crystallite sizes in the direction perpendicular to the lattice planes were calculated using the Debye–Scherrer equation with $t = \frac{K\lambda}{\beta \cos \theta_{hkl}}$, where t is the crystallite size (nm), K is Scherrer's number (usually taken as 0.9), λ is the incident wavelength (0.1542 nm), β is the full width at half maximum (FWHM) value of the peak and θ_{hkl} is the Bragg angle of the peak. Let us note that the particles are mainly composed of stacked crystallites; thus, sizes observed by scanning electron microscopy (SEM) analyses are expected to be higher than those calculated using the Debye–Scherrer formula.

Surface morphology was studied by SEM with secondary electron imaging, using Tescan Mira 3 equipment (Gaithersburg, MD, USA). Synthesized LDH slurries, obtained at pH 7, 8, 9 and 11, were diluted 100 times in water. Then, 30 μ L of the diluted suspension was deposited on sample holders and dried at room temperature. Compared to freeze drying, which is responsible for the aggregation/agglomeration of LDH particles, such a procedure results in a very thin film of preserved particles in a broad range of orientations, which provides high-quality images, allowing for the exploration of basal faces as well as particle thicknesses. This way of preparation resulted in a better characterization of the particle morphology.

Atomic absorption spectroscopy (AAS) analyses by means of a Spectra AA 220 FS VARIAN instrument (Le Plessis-Robinson, France) were used in order to quantify the amount of remaining metal cations in the filtered (0.1 μ m) and acidified (pH < 1) supernatant.

FTIR transmission spectroscopy (Bruker Equinox 55 FTIR spectrophotometer) was performed in the range 4000–400 cm^{-1} on pellets prepared using 150 mg of KBr and 0.5 mg of solid powder, which were pressurized using a manual hydraulic press of 10 tons (Grasbey Specac, Orpington, UK).

Ultraviolet–visible (UV–visible) spectrophotometric measurements were performed using a Varian UV/visible Cary 50 spectrophotometer and a cuvette of 10 mm for path optical length. It was used for iron speciation determination. A UV–visible spectrum of $[(C_{12}H_8N_2)_3Fe]^{2+}$ complex was recorded in the range from 800 to 300 nm for Fe concentrations ranging from 1 to 5 $\text{mg}\cdot\text{L}^{-1}$. For this purpose, Fe^{III} standard solutions were diluted in a reducing and a complexing acetate buffer of 0.1 M and pH 5.6. Hydroxylamine was used as an Fe^{III} reducer and 1,10-phenanthroline as a stable Fe^{II} complexing agent. The reducing and complexing buffer consists of 25 mL of the acetate buffer containing 0.2 $\text{g}\cdot\text{L}^{-1}$ of 1,10-phenanthroline and 14 $\text{g}\cdot\text{L}^{-1}$ of hydroxylamine. The calibration curve was established by plotting the absorbance measured at $\lambda_{Max} = 510$ nm versus the Fe^{2+} concentration. For solid analyses, 10 mg of solids was dissolved into 10 mL of HNO_3 4% ($36.14 \text{ g}\cdot\text{L}^{-1} \approx 0.57 \text{ mol}\cdot\text{L}^{-1}$). Then, 700 μ L of the latter solution was added to 25 mL of the

complexing buffer with or without 1,10-phenanthroline. Fe^{II} was determined in the absence of hydroxylamine. The total Fe was determined in the presence of 1,10-phenanthroline. Following Beer–Lambert law, the absorbance coefficient ϵ was deduced from the slope of the plotted absorbance calibration curve at $\lambda_{\text{Max}} = 510 \text{ nm}$ as a function of the molar concentration of $[(\text{C}_{12}\text{H}_8\text{N}_2)_3\text{Fe}]^{2+}$ and is equal to $12,048 \text{ mol}\cdot\text{L}^{-1}\cdot\text{cm}^{-1}$ with $R^2 = 0.9995$.

2.4. Geochemical Modeling

The PHREEQC[®] (Orleans, France) geochemical code was used for thermodynamic investigation based on the associated THERMOCHEM[®] (Orleans, France) thermodynamic database generated by BRGM. The geochemical model predicted the evolution of the species concentration during the modeled titration of dissolved $\text{Co}(\text{NO}_3)_2$ (0.15 M) and $\text{Fe}(\text{NO}_3)_3$ (0.05 M) by the alkaline titrant solution of NaOH (2.80 M) and Na_2CO_3 (0.78 M) at $35 \text{ }^\circ\text{C}$, according to equilibria with ferrihydrite 2 line, ferrihydrite 6 line and $\text{Co}(\text{OH})_2$ (Figure S1). The conductivity values were calculated according to the following formula:

$$\text{Conductivity (at } T \text{ }^\circ\text{C)} = ([C] \times \Lambda^\circ\text{m}) \times (1 + 0.02 \times (T - 25))$$

where $[C]$ is the concentration of the involved species in $\text{mol}\cdot\text{m}^{-3}$, $\Lambda^\circ\text{m}$ is the value of the ionic conductivity at $25 \text{ }^\circ\text{C}$ and at infinite dilution ($\Omega^{-1}\cdot\text{m}^2\cdot\text{mol}^{-1}$) and T is the temperature in $^\circ\text{C}$.

The shape of the modeled conductivity is not in agreement with data measured during the experimental titration. Indeed, the conducted modeling does not take into account the thermodynamic data related to adsorption of Co^{2+} on ferrihydrite and Na^+ on precipitates nor coprecipitation of LDHs, because these data are absent in the database used. However, the intercomparison between experimental and modeled titrations enabled interpretation of the different phenomena that take place during the experimental titration.

3. Results and Discussion

3.1. Titration

Figure 1 shows an example of the titration curve of the mixed $\text{Co}(\text{NO}_3)_{2(\text{aq})}$ (0.15 M) – $\text{Fe}(\text{NO}_3)_{3(\text{aq})}$ (0.05 M) solution by the alkaline titrant solution from the initial pH to 11.

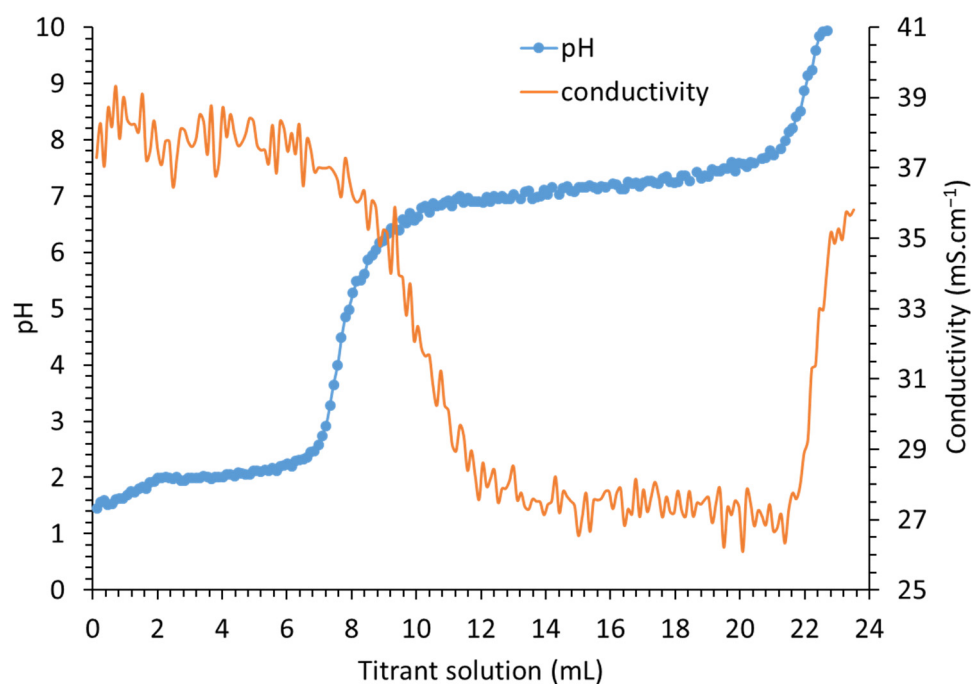


Figure 1. Titration curve of 100 mL of a solution containing the cations mixture Co^{2+} (0.15 M) and Fe^{3+} (0.05 M) using the alkaline titrant solution of NaOH (2.80 M) and Na_2CO_3 (0.78 M).

The initial media solution is acidic (pH~1.8) due to the constituent cations, which behave as weak Bronsted acids and consequently have the ability to produce hydronium (H_3O^+ or H^+ _(aq)) ions. This acidity is a function of the size, charge and electronegativity of the cations. The smaller the cation and the higher the electronegativity of the metal ions, the more acidic it will be [50].

When adding the first drops of the alkaline titrant into the solution of the metallic cations, pH increases slowly, in agreement with H^+ consumption by both OH^- and CO_3^{2-} (for the formation of H_2O and H_2CO_3 , respectively). Fe^{3+} hydrolysis begins (into $\text{Fe}(\text{OH})_2^+$ and $\text{Fe}(\text{OH})_2^+$) at the same time. At pH~2.1, pH reaches a first pseudo-plateau in agreement with the simultaneous precipitation of Fe^{III} . At around pH~2.3, the precipitation of Fe^{3+} is mostly complete. This first pH plateau is followed by a rapid increase in the pH until 4.1–4.3, i.e., rapid consumption of H^+ mainly by free OH^- and CO_3^{2-} . Beginning from this pH range, HCO_3^- appears, and the equivalent point of the $\text{H}_2\text{CO}_3/\text{HCO}_3^-$ acid–base couple is reached at 6.4. From this point, another pseudo-buffered area starts in agreement with Co hydroxylation, which is responsible for the progressive coprecipitation of the metallic cations. The progressive enrichment in Co into the coprecipitated material induces positive charges, which are compensated for by the intercalation of hydrated anions, resulting in LDH formation [30,31]. At around pH~9.0, Co/Fe LDH co-precipitation is complete. The equivalent points of the $\text{HCO}_3^-/\text{CO}_3^{2-}$ acid–base couple are reached at the pH value of 11. Finally, while the alkaline titrant solution addition is carried out, pH increases up to the pH value of the alkaline solution itself (pH > 11).

According to the ionic composition of the metallic solution, at pH 1.7 and at 35 °C, the conductivity should be equal to $69 \text{ mS}\cdot\text{cm}^{-1}$, in which NO_3^- accounts for $38.6 \text{ mS}\cdot\text{cm}^{-1}$, H^+ for 8.5, Fe^{3+} for 12 and Co^{2+} $9.90 \text{ mS}\cdot\text{cm}^{-1}$.

The initial measured conductivity was $38 \text{ mS}\cdot\text{cm}^{-1}$ because the concentration of the dissolved salts exceeds 10^{-2} M , which is the highest limit of applicability for Kohlrausch's law. Nevertheless, conductivity was used as an indicator to investigate the evolution of the physical and chemical parameters during titration. The recorded conductivity is plotted in Figure 2 (orange line) versus the added volume of alkaline titrant solution.

For better insight, Figure 2 highlights the conductivity variations versus pH values, showing that conductivity greatly fluctuates in the pH ranges 1.8–2.6 during Fe^{III} precipitation (Figure S1) and 6.6–7.8 during LDH coprecipitation. Such unpredictable behavior clearly shows the effects of the concomitant phenomena-inducing transfer of ionic species into solution, in agreement with rapid and instable precipitation–dissolution phenomena. During titration, conductivity is dominated by the presence of NO_3^- , whose concentration (0.45 M) does not significantly evolve over time (Figure S1).

As the conductivity linked to the concentration of NO_3^- anions is constant over time, the observed conductivity decrease in the range from 1.8 to 2.6 should predominantly be related to Fe^{3+} precipitation and, to a lesser extent, to H^+ neutralization by the added OH^- and Na^+ , whose concentrations continuously increase (Figure S1). In the pH range from 2.3 to 3.3, the H^+ neutralization that proceeds should be the only phenomenon weakly influencing conductivity. According to the decrease in cobalt concentration from pH 2 to 9 (Figure 2A), it is apparent, from Figure 2B, that Co^{2+} concentration is responsible for the evolution of the conductivity value. From pH > 2 (Figure 1, orange line), in comparison with Figure S1, any significant decrease in conductivity is thus related to Co^{2+} behavior. The increase in conductivity should be related to the gradual increase in Na^+ concentration and the increase in total inorganic carbon and, to a lesser extent, OH^- ions in the solution (Figure S1). Surprisingly, conductivity only increases from pH 8, whereas it was expected to have increased from pH 5 following the precipitation of Fe^{3+} and the neutralization of H^+ , where Na^+ concentration reached 0.2 M ($10 \text{ mS}\cdot\text{cm}^{-1}$). At pH 8, the Na^+ concentration reached 0.6 M ($34 \text{ mS}\cdot\text{cm}^{-1}$). The first decrease in conductivity is in the pH range from 2.3 to 6, and then the plateau observed from pH range 6 to 8, demonstrating that Co^{2+} is accountable for the conductivity evolution from pH 2.3 to 8. The absence of any increase in conductivity in this pH range tends to demonstrate the Na^+ sorption phenomenon.

In agreement with the literature [51], the ionic radii of cations, related to that of oxygen, determines the possibility of Na^+ insertion into an octahedral lattice without further critical distortion. A cation/ O^{II} radii ratio between 0.414 and 0.732 would indicate the possible insertion of the cation [51–53]. The ionic radius of Na^+ is 0.95 Å, and that of O^{II} in an octahedral site is 1.40 Å. Na^+ can thus be inserted into an octahedral lattice ($r(\text{Na}^+/\text{O}^{\text{II}})$ of 0.68 Å). In addition, because of the high concentration of Na^+ , it should also adsorb onto the external surfaces of Fe^{III} precipitates, in agreement with the pH values being higher than the point of zero net charge (PZNC) [54]; indeed, above PZNC, the solid surface charges are negative. In addition, in the pH range of 6–8, the increase in HCO_3^- in solution should slightly increase conductivity up to $\sim 4 \text{ mS}\cdot\text{cm}^{-1}$ (Figure S1). The stability of conductivity in such a pH range is linked to HCO_3^- intercalation into the interlamellar space of LDHs. Above pH 8, the increase in conductivity is linked to the increase in both Na^+ and CO_3^{2-} concentrations due to the addition of alkaline solution.

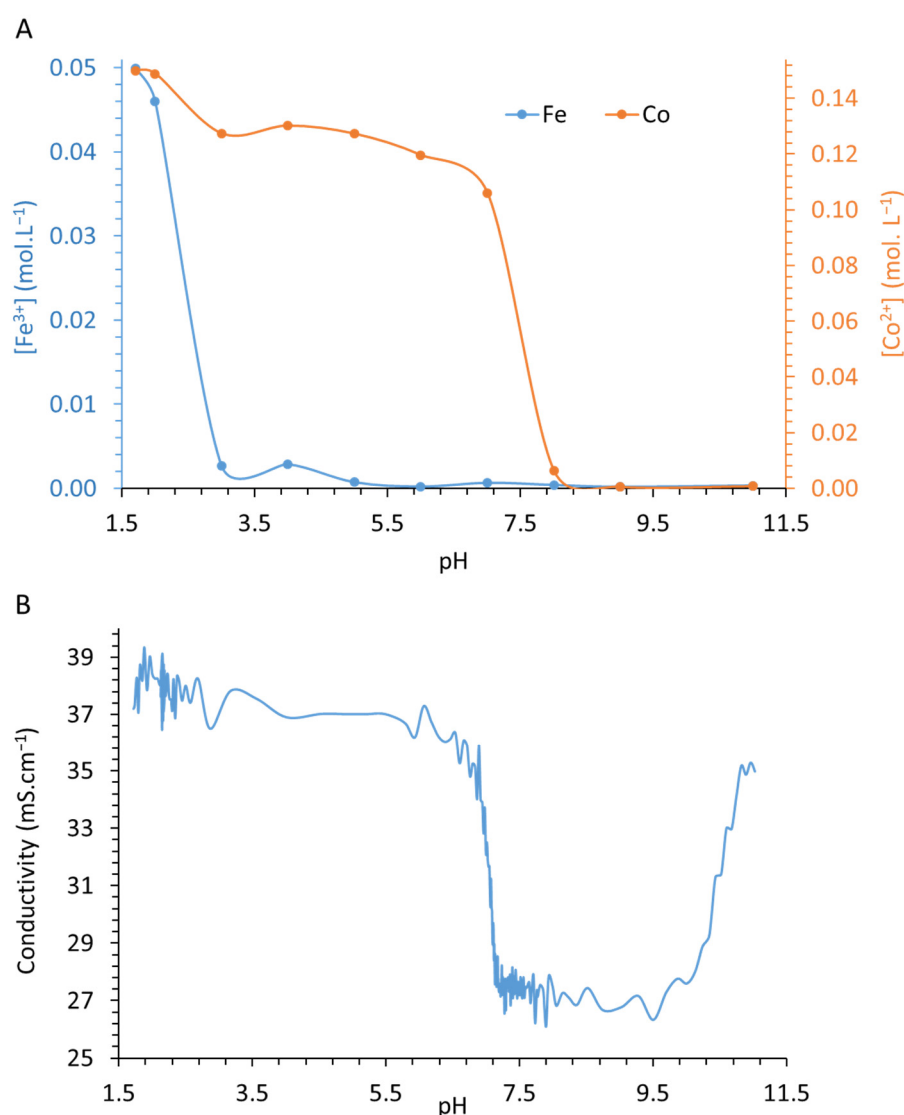


Figure 2. (A) Remaining concentrations of Fe (blue) and Co (orange) in the supernatant and (B) measured conductivity as a function of the corresponding titration pH.

3.2. Atomic Absorption Spectroscopy Analyses of Co^{2+} and Fe^{3+} in the Supernatant

For each titration pH value, the supernatant extracted from the centrifugation was analyzed by AAS to quantify the remaining amount of Co^{2+} and Fe^{3+} (Figure 2A).

A small decrease in the Fe^{III} concentration at pH 2 indicates the point at which Fe^{III} begins to precipitate. From pH 2 to 3, the sharp decrease in the Fe^{III} solution concentration

is in agreement with the precipitation of iron species. Surprisingly, the Fe^{III} concentration remains quasi-constant from pH 3 to 4 at 2.7×10^{-3} M, which is close to 5% of the initial Fe^{III} concentration. This concentration value decreases progressively and is close to zero at pH 8. According to the literature, K_s values of expected precipitated iron species are usually extremely low (10^{-44} – 10^{-37}) [55,56]. The AAS results suggest the presence of free Fe^{2+} in the media.

Regarding Co^{II} , its concentration remains constant until pH 2 (0.15 M). From pH 2 to 3, the Co^{2+} concentration sharply decreases, with a loss of 15% from the initial concentration (from 0.15 to 0.127 M). This result suggests Co^{2+} adsorption onto iron precipitates; the Co/Fe ratio in the solid, i.e., the molar ratio of adsorbed Co^{II} onto precipitated Fe^{III} , reaches 1/2. From pH 3 to 5, the Co^{II} concentration remains constant. Beyond this pH value, the Co^{II} concentration decreases progressively; the speed of this Co^{II} concentration decrease accelerates from pH 7 to 8. In the pH range between 2.3 and 8.0, the decreasing evolution of the remaining Co^{II} in the solution is synchronous with the conductivity values. The Co^{II} concentration is close to 0 from pH 9. Measurements of Co^{2+} concentration by AAS and of conductivity enable the calculation of Co^{2+} concentration over time (Figure S2).

3.3. PXRD Characterization of Solids Synthesized by Acid–Base Titration

Solids obtained after each of the nine partial titrations were characterized by PXRD to determine the nature of the obtained crystalline phases (Figure 3); when the LDHs were obtained, their lattice parameters were calculated using the Rietveld refinement method (Table 1).

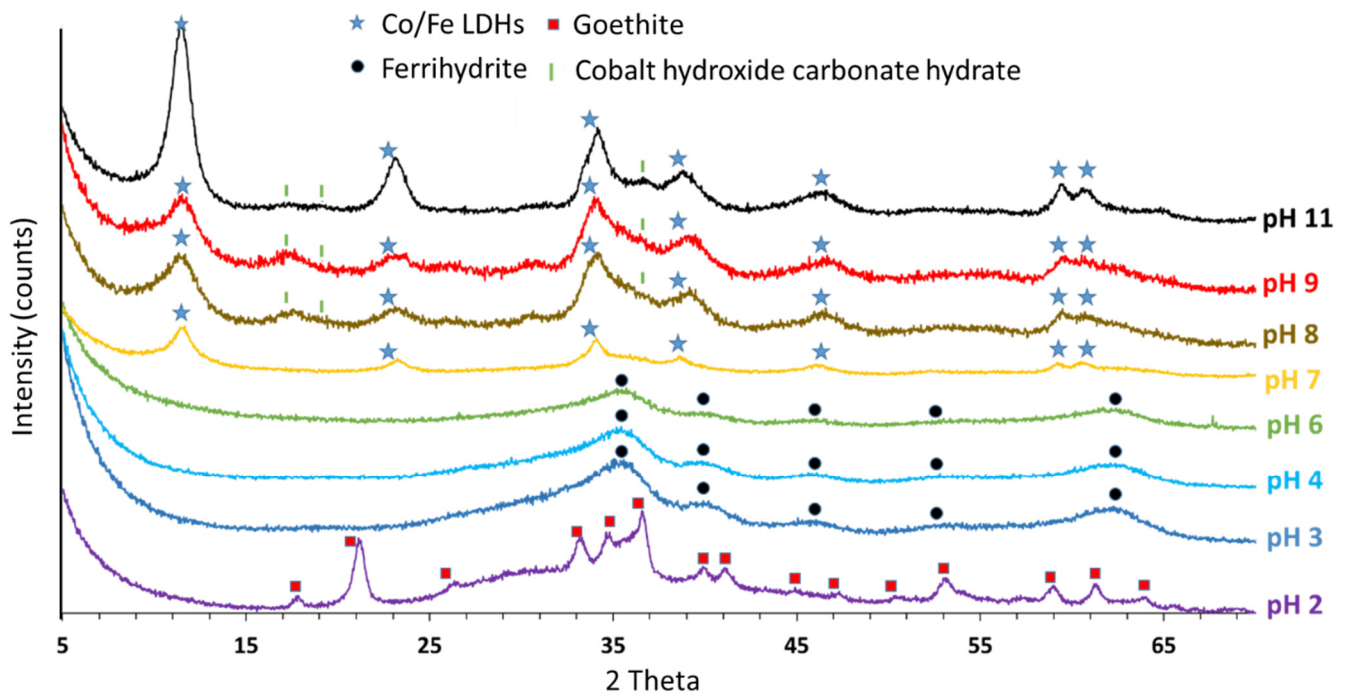


Figure 3. PXRD pattern for solids collected after titrating the starting solution up to the reported pH values.

Table 1. XRD data provided by the Rietveld refinement method for the solids obtained from pH 7 to 11.

Characterization Data for Solid Obtained from pH 7 to 11				
pH of synthesis	7	8	9	11
LDH species	2	2	2	2
$d(003)$ (Å)	7.64–7.68	7.64–7.64	7.63–7.63	7.63–7.69
c parameter (Å)	22.92–23.04	22.92–22.91	22.90–22.90	22.89–23.06
a parameter (Å)	3.12–3.09	3.11–3.10	3.08–3.11	3.11–3.09
t crystallite size (nm)	12.20–3.20	6.78–3.19	6.00–1.80	10.06–5.29
LDH species relative content (%)	14–86	22–78	16–83	62–38

As revealed by PXRD, goethite is the main mineral phase obtained at pH 2 (JCPDS 01-073-0522 (I)), in agreement with diffraction peaks located at 17.85° , 21.1° , 33.16° , 34.62° and 36.58° , which enable us to calculate d_{hkl} . From the collected XRD data and the orthorhombic crystalline system, the calculated lattice parameters ($a = 4.38$ Å, $b = 9.93$ Å, $c = 3.10$ Å) are in agreement with the literature [57]. The goethite diffraction bands are superimposed on two wide diffraction bumps in the range from 25° to 45° and in the range from 55° to 70° , showing the presence of a poorly crystalline ferrihydrite phase. Indeed, ferrihydrite is a form of iron oxyhydroxide, which usually forms in the course of iron mineralization with relatively poor crystallinity [58]. Ferrihydrite is thermodynamically unstable and can readily recrystallize to goethite, magnetite and lepidocrocite [58–60]. The presence of goethite is in agreement with the thermodynamic transformation of ferrihydrite to goethite and is probably linked to washing and/or drying steps.

From pH 3 up to 6, poorly crystalline ferrihydrite is the only phase evidenced by PXRD diffraction peaks located at 35.42° , 39.87° , 45.61° , 52.81° and 62.09° , in agreement with (JCPDS 01-073-8408). The obtainment of ferrihydrite in such a range of pH values clearly demonstrates the artefact observed at pH 2, which is related to the transformation of metastable ferrihydrite to goethite. Ferrihydrite is thus the pristine reactional intermediate.

According to Maillot et al. [61], ferrihydrites synthesized in this study are 5 line structures, at pH 3 and 4; a 4 L structure was observed at pH 6. This change in crystallinity between the so-called 2 line and 6 line ferrihydrite is generally interpreted as a change in mean particle size from 2 to 6 nm, respectively [62–64].

The higher the pH, the lower the relative intensity of diffraction bands, i.e., the lower the ferrihydrite crystallinity. From pH 3 to 6, ferrihydrite particle size is calculated from the peak at 35° . It is 9.3, 7.4 and 3.2 nm at pH 3, 4 and 6, respectively. The higher the pH, the smaller the particle size.

Ferrihydrite features small particle sizes and a large specific area. It is, moreover, modeled as a mixture of a defect-free phase and a defective phase, which ranges from 33 to 50% in a 6L ferrihydrite [65]. Ferrihydrite is thus well-known and used for its high surface reactivity, such as in metal adsorption [66–68], probably due to the presence of the defective phase. Moreover, the ability to bind metal was demonstrated to slow down [69] and impede [70] the rate of ferrihydrite transformation into other crystalline iron phases. Such behavior is also explained by metal substitution [71,72] in the ferrihydrite structure during dissolution–reprecipitation phenomena. In comparison with the evolution of ferrihydrite into goethite observed at pH 2, and in agreement with the results provided by AAS and conductivity in the pH range 3–6, the maintenance of the ferrihydrite structure is attributed to the presence of both Na^+ and Co^{2+} in the medium, which can adsorb onto ferrihydrite. As previously discussed, Na^+ can insert into octahedral lattices and/or bind onto the negatively charged $=\text{M}-\text{O}^-$ surface sites of ferrihydrite. Co^{2+} (ionic radius 0.072 Å) may be able to substitute Fe^{3+} (ionic radius 0.067 Å) in agreement with dissolution–reprecipitation phenomena. Co^{2+} adsorption onto negatively charged $=\text{M}-\text{O}^-$ surface sites is, nevertheless, the most kinetically probable hypothesis. Both Co^{2+} and Na^+ compete for such adsorption sites. The cation-exchange process favors the uptake of divalent over monovalent species.

Co^{2+} is thus the predominant sorbed cation until Na^+ reaches a concentration value high enough to compete with Co^{2+} . It is thus assumed that both Co^{2+} and Na^+ sorption on the negatively charged $=\text{M}-\text{O}^-$ surface sites of ferrihydrite nuclei generate passivation layers, which significantly slow down the degradation of ferrihydrite to goethite by limiting the iron transfer between sites.

From pH 7, PXRD patterns show characteristic Co/Fe LDH structures [73–75] associated with some impurities. The reflection peaks at 17.5° , 20.0° , 24.2° , 26.7° , 33.8° , 35.4° and 39.5° are characteristic of $\text{Co}(\text{CO}_3)_{0.5}(\text{OH})\cdot 0.11 \text{H}_2\text{O}$ (JCPDS 00-048-0083) and those at 18.4° , 30.2° , 35.6° , 37.2° , 43.2° , 53.6° and 57.2° are characteristic of the Co/Fe-based spinel structure in the solid (JCPDS 01-083-6167). The position of the LDH diffraction peaks, indexed in Table 1, are in agreement with a hexagonal structure (JCPDS 04-017-8816).

The Rietveld refinement method applied to the XRD pattern (Figure S3) indicates that the materials synthesized at pH 7, 8, 9 and 11 are composed of a 73% LDHs and 27% spinel phase; 54% LDHs, 41% cobalt hydroxycarbonate hydrate and 5% spinel phase; 53% LDHs, 43% cobalt hydroxycarbonate hydrate and 4% spinel phase; 70% of LDHs, 24% cobalt hydroxycarbonate hydrate and 6% spinel phase. In the range from pH 8 to 9, the passivation phenomenon induced by Na^+ sorption onto the negatively charged $=\text{M}-\text{O}^-$ surface sites of LDH nuclei could be responsible for the precipitation of cobalt hydroxycarbonate hydrate impurities. This adsorption phenomenon is supported by the characteristic constancy of the conductivity values in the pH range 7–9.5. From pH 9 to pH 11, Ostwald maturation through the dissolution–reprecipitation phenomena, which progresses with time and with the addition of alkaline solution [28,76,77], is probably responsible for the increase in both LDH content and crystallinity.

The (110) peaks at $\sim 59^\circ$ allowed for the determination of the a lattice parameter value, which is equal to double the distance at (110); $a = 2 \times d(110)$. This value is directly related to the distance between adjacent cations in the LDH structure. The variation in synthesis pH did not have any effect on the value of the ' a ' lattice parameter, which was constant at $3.10 \pm 0.10 \text{ \AA}$ from pH 7 to 11.

The (003) peak at $\sim 11^\circ$ allowed for the determination of the basal spacing (c'), as d_{003} is directly equal to the thickness of one brucite-like layer and interlayer spacing. As shown in Table 1, d_{003} remains constant with the increase in the pH synthesis value; the interlayer space c' ranges between 7.63 and 7.69 \AA . According to the literature, the basal spacings correspond to a predominant CO_3^{2-} interlayer anionic species [18].

Moreover, the positions of the reflections (012)–(015) at intermediate angles (35° – 45°) help in calculating the c parameter using the equation linking the Miller indices to the lattice parameter in a hexagonal crystalline system [74]. The ratio between the c parameter and the c' reflects the layer periodicity along the c axis. For the solids obtained at pH 7, 8, 9 and 11, the ratios are 2.91, 2.92, 2.91 and 2.94, respectively. In agreement with the literature [1], convergence of the c/c' ratio to 3 reflects the perfect periodicity along the c axis at a structural scale and confirms the homogeneous distribution of interlayer anion species.

Regardless of the pH, two groups of crystalline LDH particles were identified: a group of pseudo-crystallized particles in which crystallite sizes range from 1.8 to 5.3 nm, and a group of crystallized particles in which crystallite sizes range from 6.0 to 12.2 nm. Their rather different apparent sizes, i.e., 4.46, 3.98, 2.54 and 8.25 nm for pH 7, 8, 9 and 11, respectively, influence the apparent crystallinity of the solid. The decrease in the apparent crystallite sizes from pH 7 to 9 is in agreement with the incorporation of residual Co^{II} into the pristine LDHs precipitated at pH 7. From pH 9 to pH 11, the increase in the apparent crystallite size is in agreement with the Ostwald maturation phenomenon through the dissolution–reprecipitation phenomena, which progresses with time and the addition of the alkaline solution [28,76,77].

3.4. LDH Characterization after Aging at Room Temperature

Prior to any characterization, the pH values of the slurries were measured; the exact pH values were 6.98, 7.96, 8.97 and 10.95. The slurries were buffered by the synthesized LDHs.

3.4.1. PXRD of the Solids Collected after Aging at Room Temperature

Figure 4 shows the LDH PXRD patterns after aging at room temperature for 700 days, and Table 2 presents the lattice parameters calculated using the Rietveld refinement method (Figure S4).

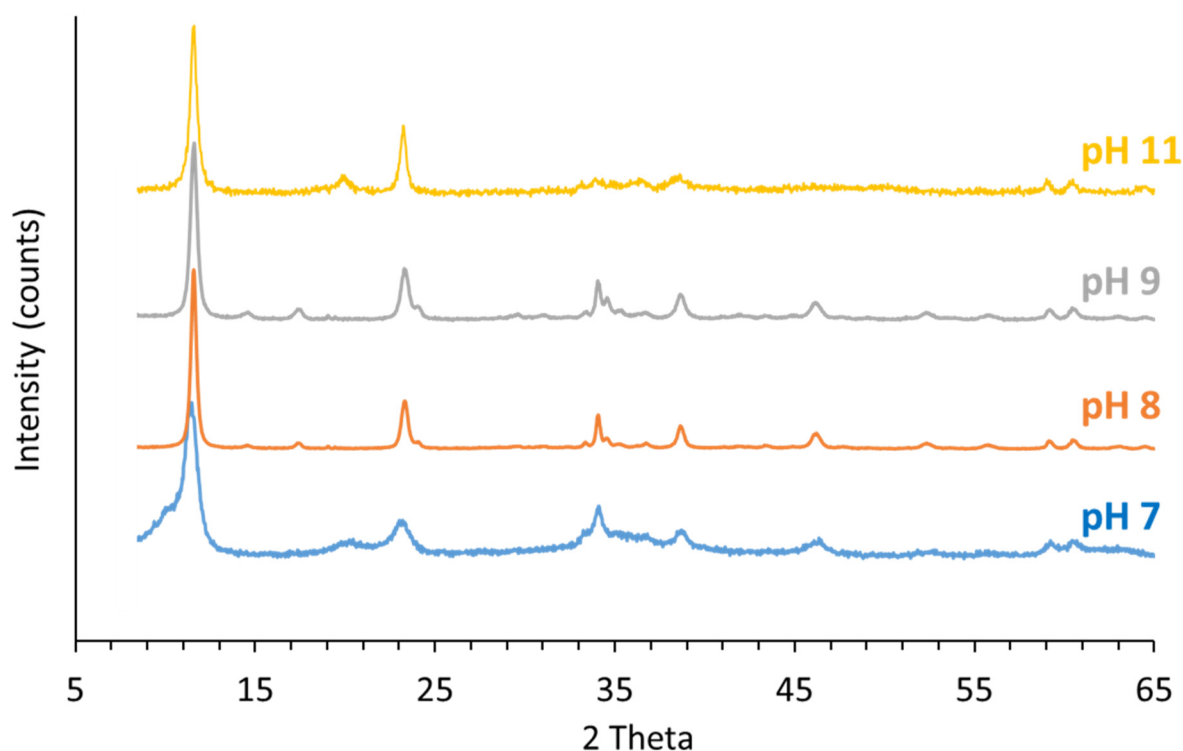


Figure 4. PXRD pattern of the solids collected after aging.

Table 2. XRD data provided by the Rietveld refinement method for the solids obtained from pH 7 to 11 after aging.

Solids Obtained from pH 7 to 11				
pH of synthesis	7	8	9	11
LDH species	3	2	2	3
$d(003)$ (Å)	7.62–7.71–8.71	7.61–7.63	7.60–7.63	7.66–7.65–7.72
c parameter (Å)	22.86–23.13–26.14	22.84–22.86	22.63–22.90	22.97–22.95–23.15
a parameter (Å)	3.12–2.96–3.07	3.12–3.12	3.12–3.12	3.22–3.13–3.06
t crystallite size (nm)	16.28–8.14–4.88	52.89–23.12	43.36–19.41	51.57–16.45–4.94
LDH species relative content (%)	34–18–48	84–16	87–13	4–17–79

As previously observed, PXRD patterns show characteristic Co/Fe LDH structures [73–75]. The persistence of cobalt hydroxycarbonate hydrate was demonstrated for materials synthesized at pH 8 and 9. At pH 11, the reflection peaks at 20.6° , 37.0° , 48.9° and 50.8° are characteristic of CoO(OH) (JCPDS 01-072-2280), and those at 18.5° , 30.4° , 35.8° , 37.5° , 43.5° , 54.0° and 57.5° are characteristic of a cobalt-based spinel structure in the solid (JCPDS 01-083-6167).

The Rietveld refinement method applied to the XRD pattern (Figure S4) indicated that the material synthesized at pH 7 is composed of 100% LDHs. At pH 8 and 9, 69% and 58%

of the synthesized materials are LDH materials, respectively, and the rest are composed of cobalt hydroxycarbonate hydrate. At pH 11, the synthesized material is composed of 75% Co/Fe LDH, 21% cobalt iron oxyhydroxides and 4% cobalt-based spinel phase.

The LDH basal spacings, ranging from 7.60 to 7.71 Å, are correlated with the predominance of CO_3^{2-} as anionic species in the interlayer space [18]; the d_{003} value of 8.71 Å obtained at pH 7 is in agreement with the predominance of NO_3^- species [1].

Regardless of the investigated pH, aging favors crystallinity. Particle sizes are drastically increased at pH 8 and 9, which tends to demonstrate that the higher the defect contents, the higher the degree of Ostwald maturation, which also favors particle growth.

3.4.2. Scanning Electron Microscopy (SEM) of Co/Fe LDHs Synthesized at pH 7, 8, 9 and 11

Figure 5 shows SEM secondary electron imaging of the Co/Fe LDHs synthesized at pH 7, 8, 9 and 11.

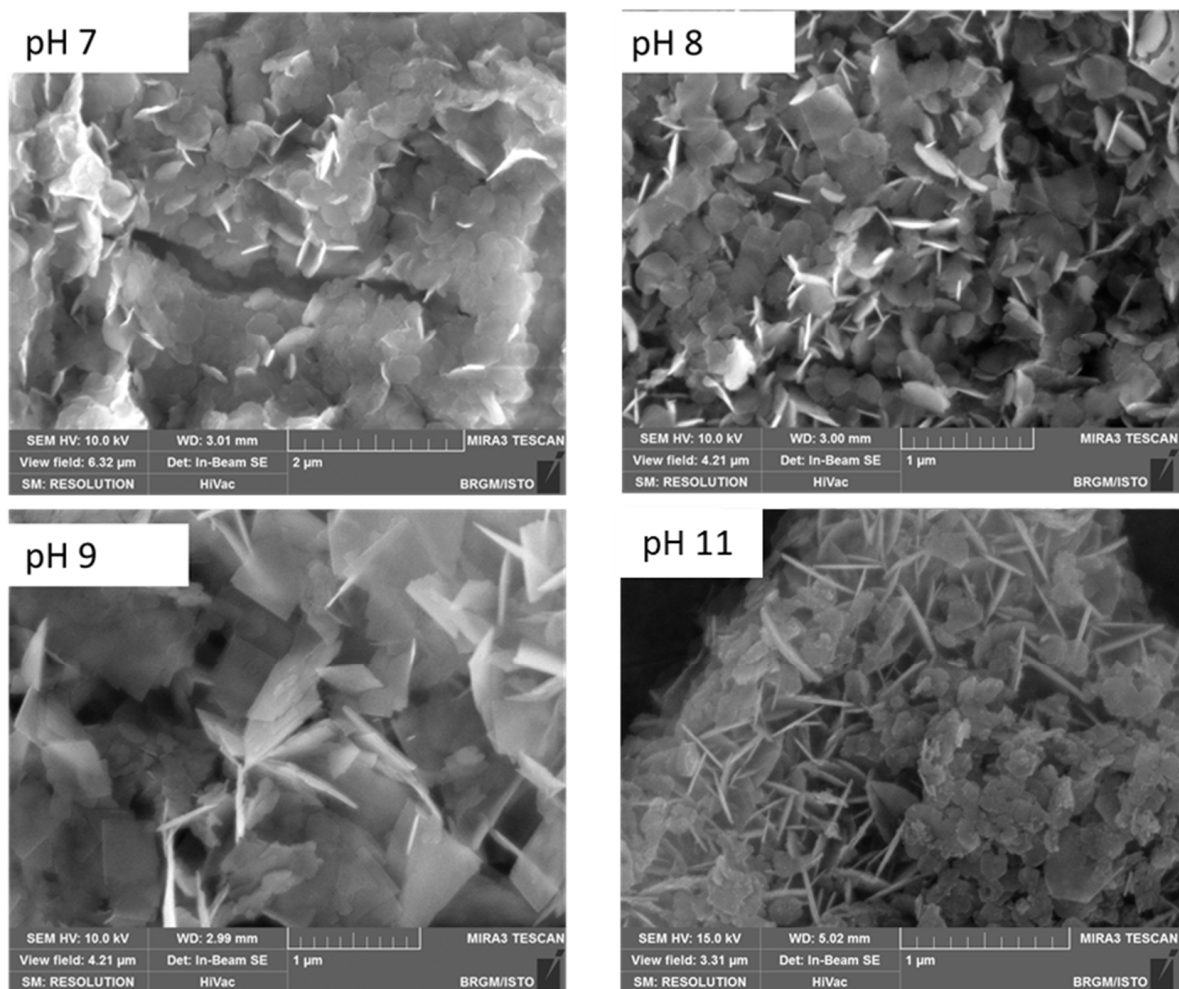


Figure 5. SEM images for Co/Fe LDHs synthesized at pH values 7, 8, 9 and 11.

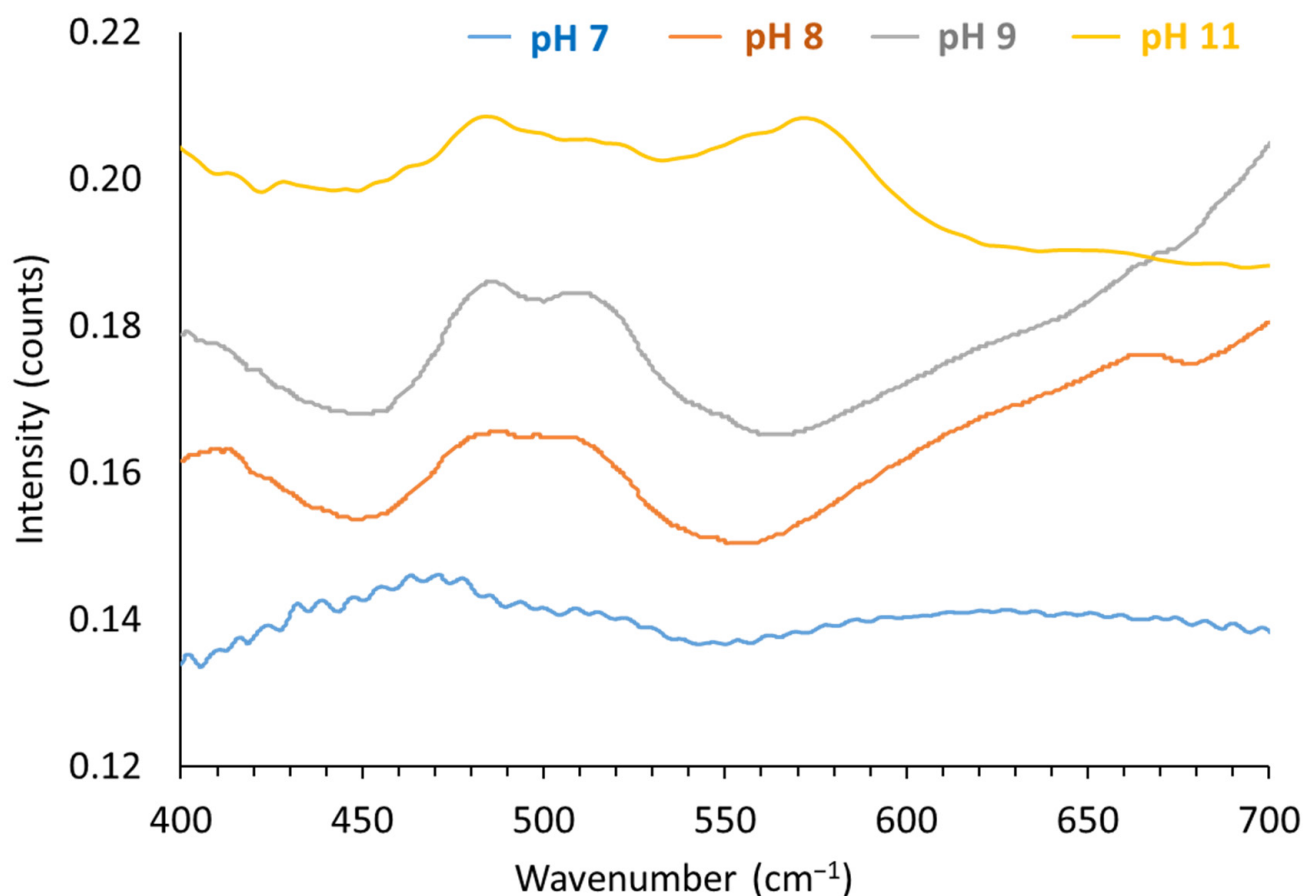
The Co/Fe compounds resulting from synthesis at pH values 7, 8, 9 and 11 are composed of agglomerated platelet particles presenting a pseudo-hexagonal shape. The hexagonal morphology of these particles is in good agreement with the usual morphology of LDH particles [78–80]. The particles show hexagon side lengths from 100 to 500 nm and thicknesses between 10 and 50 nm (Table 3).

Table 3. LDH particle thickness and length versus pH.

pH	LDH Thickness (nm)	LDH Length (nm)
7	31–36	170–290
8	11–44	180–400
9	27–47	475–510
11	23–42	100–300

3.4.3. FTIR Spectra of the LDHs Synthesized at pH 7, 8, 9 and 11

Figure 6 shows the FTIR spectrum of the LDHs synthesized at pH 7, 8, 9 and 11 in the range from 400 to 800 cm^{-1} .

**Figure 6.** FTIR spectrum of the LDHs synthesized at pH 7, 8, 9 and 11 in the range from 400 to 800 cm^{-1} .

Two characteristic peaks are associated with the presence of Co/Fe LDH in the solid: 490 cm^{-1} for Fe–O and 515 cm^{-1} for Co–OH vibrations [81,82]. The higher the crystallinity, the better the band resolution. The band at 575 cm^{-1} is characteristic of Co–O vibration in Co–O(OH) [83]. The presence of the Co-based spinel is manifested by the characteristic Co–O vibration bands at 553 and 655 cm^{-1} [82,84,85].

Figure 7 shows the FTIR spectrum of the LDHs synthesized at pH 7, 8, 9 and 11 in the range from 1800 to 1100 cm^{-1} .

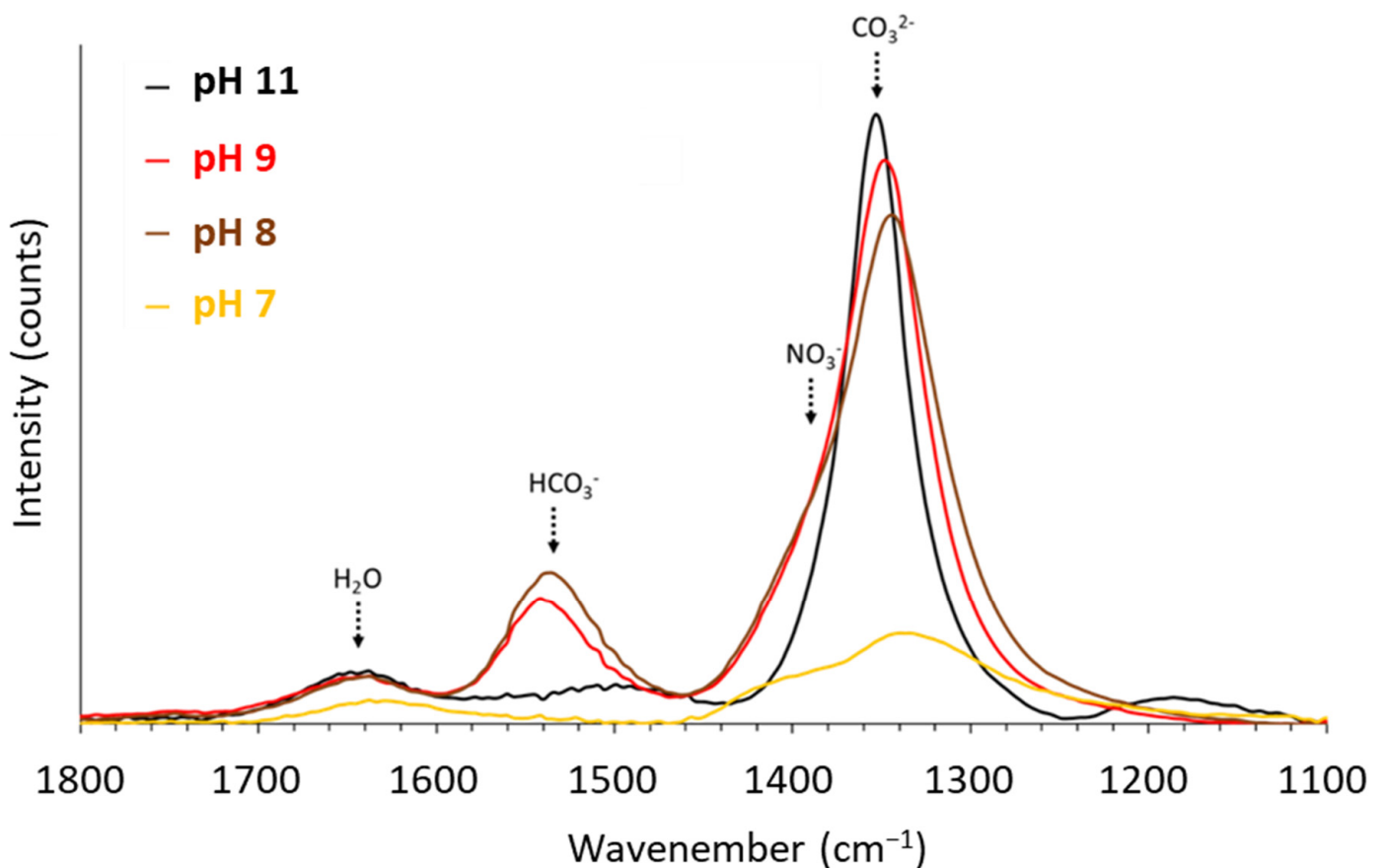


Figure 7. FTIR spectra obtained for the solid collected after the titrations were carried out until reaching pH values 7, 8, 9 and 11.

The bands observed at 1640, 1540, 1380 and 1352 cm^{-1} are related to the presence of interlamellar water [86], hydrogenocarbonates (HCO_3^-) [12,30], nitrates (NO_3^-) and carbonates (CO_3^{2-}) [12,87–90], respectively. Surprisingly, NO_3^- and CO_3^{2-} are the only interlamellar anions observed at pH 7. As it is quite difficult to differentiate the hydroxyl anions in FTIR, OH^- could be the predominant interlamellar anion. From pH 8 to 11, the FTIR spectra show a drastic increase in both $\text{CO}_3^{2-}/\text{NO}_3^-$ and $\text{CO}_3^{2-}/\text{HCO}_3^-$ band ratios, while the $\text{NO}_3^-/\text{HCO}_3^-$ band ratio decreases. Data provided by FTIR support that HCO_3^- is predominant at pH 8 and 9, while CO_3^{2-} is the predominant interlamellar anion at pH 11.

3.4.4. UV–Visible Absorbance of Various Contents of Fe and Synthesized LDHs

Figure 8 shows the plotted UV–visible spectra of 1, 2, 3, 4 and 5 $\text{mg}\cdot\text{L}^{-1}$ standard solutions of $[(\text{C}_{12}\text{H}_8\text{N}_2)_3\text{Fe}]^{2+}$ complex (dotted lines). It also shows the UV spectra of the dissolved Co/Fe LDHs synthesized at pH values 7, 8 and 9 (solid lines). The measurements were conducted in the presence or the absence (mentioned “without R”) of the Fe^{III} reducing agent from 325 to 625 nm.

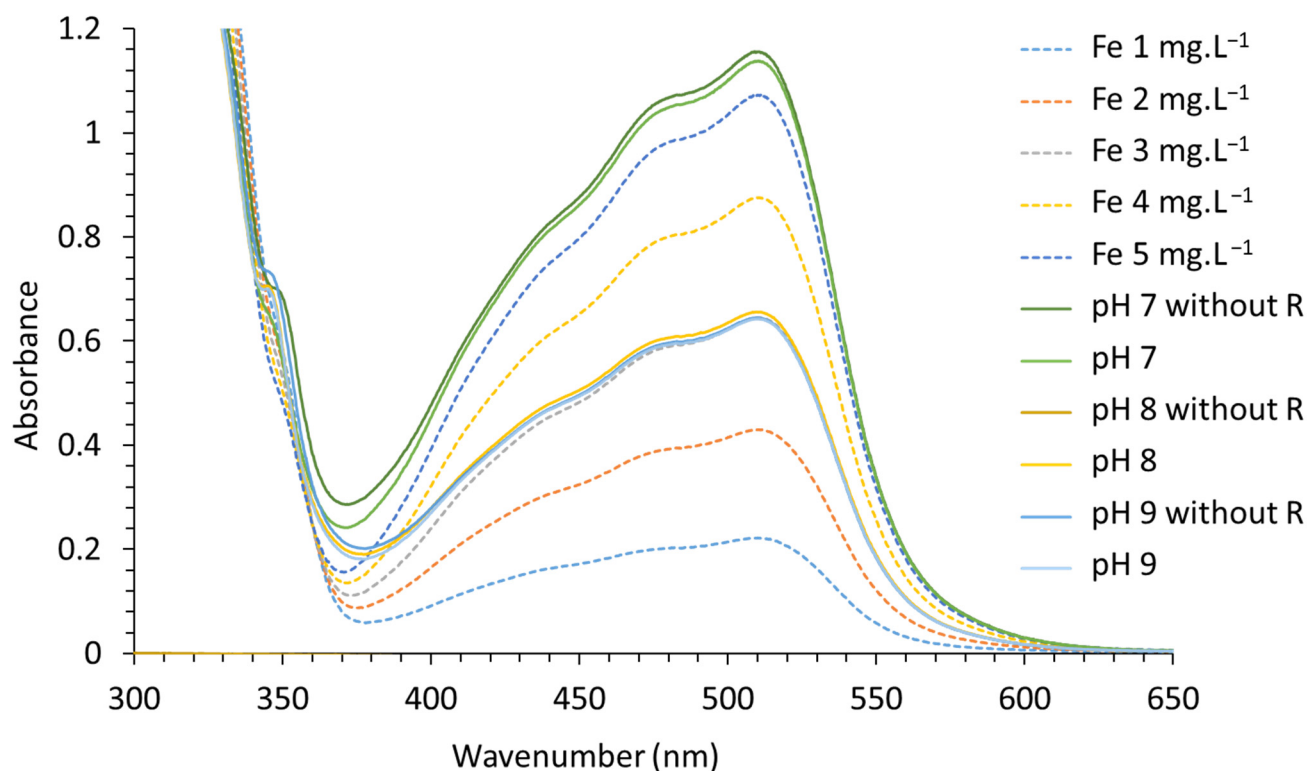


Figure 8. UV-visible absorbance of various concentrations of Fe and synthesized LDHs, with and without the Fe^{III} reducing agent.

The $[(C_{12}H_8N_2)_3Fe]^{2+}$ complex spectra present four absorption bands at 511, 476, 440 and 408 nm [91], which are characteristic of a low spin complexed Fe^{II}. The absorbance recorded for the dissolved LDHs shows the same shape as the analyzed $[(C_{12}H_8N_2)_3Fe]^{2+}$ complex, regardless of the analyzed sample and whether Fe^{III} reducing agent is present or absent. These results tend to demonstrate that all the LDH-iron is present as Fe^{II}. Nevertheless, the addition of Co^{II} to a $[(C_{12}H_8N_2)_3Fe]^{3+}$ complex standard solution, in which $(C_{12}H_8N_2)_3$ complexes Fe^{III} at concentrations equimolar to Fe^{III}, is responsible for the progressive total reduction of $[(C_{12}H_8N_2)_3Fe]^{3+}$ to $[(C_{12}H_8N_2)_3Fe]^{2+}$, which strongly colors the solution.

In any case, the Fe^{II} concentration in the solutions is two times greater when prepared from LDHs synthesized at pH 7 than from LDHs synthesized at pH 8 and 9. These results are in good agreement with AAS measurements conducted on the LDH synthesis supernatants and support the identity of the LDHs synthesized at pH 7 as being M^{II}/M^{III} 2/2 and those at pH 8 and 9 as being 3/1.

4. Discussion

The monitoring of pH and conductivity carried out during titrations completed by the PXRD characterizations of solids, UV-visible characterization of dissolved solids and AAS analyses on the supernatants allowed for the determination of the speciation of intermediates involved in the pathway to Co/Fe LDH formation.

From pH 1.8 to 2.6, there is precipitation of the trivalent cation Fe^{III}. In the pH range 1.8–6, the formation of ferrihydrite was confirmed. Co²⁺ and Na⁺ sorption on the negatively charged =M–O[−] surface sites of ferrihydrite nuclei generate passivation layers that maintain the ferrihydrite structure by avoiding degradation to goethite via limiting of iron transfer between nuclei.

From the AAS measurements, the adsorption capacitance of the Co^{2+} on the ferrihydrite at pH 6 was evaluated using Equation (4):

$$Q = (C_0 - C_t) \times V/m \quad (4)$$

where C_0 and C_t are the initial and equilibrium mass concentrations of cobalt, V is the volume of the solution and m is the weight of the ferrihydrite deduced from precipitated iron based on the chemical formula $\text{Fe}(\text{OH})_3$ [92]. Q is the adsorption capacity, expressed in mg of sorbed Co^{2+} per g of ferrihydrite, and is equal to $220 \text{ mg}\cdot\text{g}^{-1}$ at pH 6. This result is in good agreement with the literature [66,68,93,94]. Figure 9 shows the evolution of Co^{2+} concentration versus time in the pH range from 2 to 2.2. Data were extracted from Figure S2. The data enabled the determination of the kinetic constant for Co^{2+} adsorption on ferrihydrite.

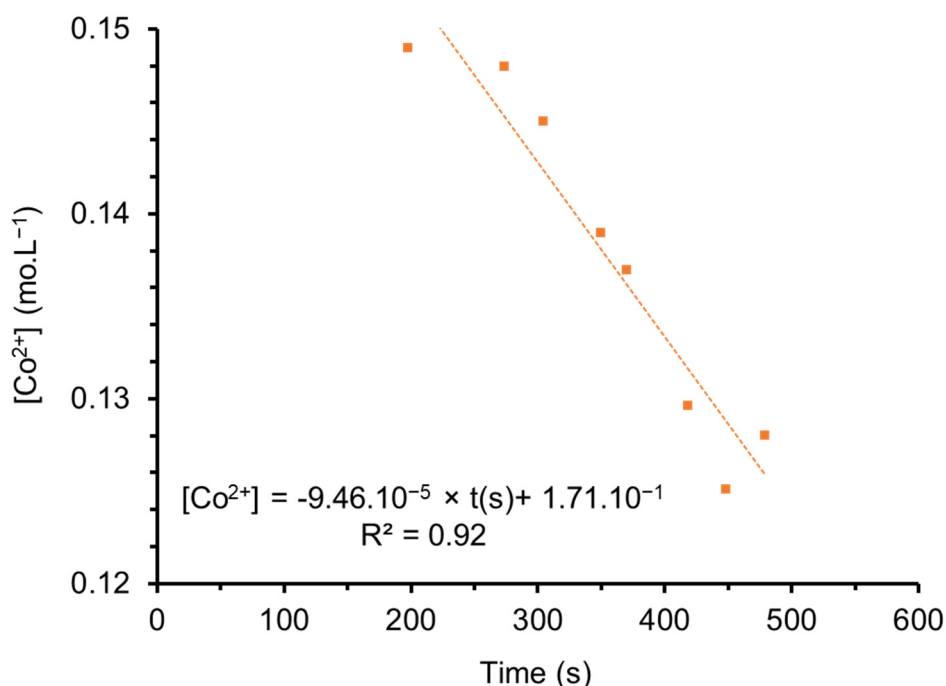


Figure 9. Evolution of the Co concentration versus time from pH 2 to 2.2. Results were provided by AAS and calculated using conductivity measurements.

Co^{2+} concentration decreases linearly versus time with a regression coefficient (R^2) of 92%.

The adsorption equilibrium kinetics of Co^{2+} on ferrihydrite is of a zero order ($\alpha = 0$); this behavior can be explained by the cobalt concentration in the solution, which is three times higher than that of Fe^{3+} . The adsorption kinetic constant is close to $1.57 \times 10^{-6} \text{ mol}\cdot\text{min}^{-1}$.

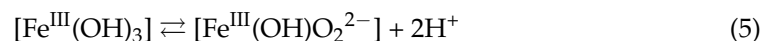
Co^{II} adsorption on ferrihydrite is responsible for the decrease in the $\text{Co}^{\text{III}}/\text{Co}^{\text{II}}$ redox potential in response to increasing pH, where Co^{II} becomes a reducing agent for Fe^{III} in ferrihydrite [92,95–98]. When sorbed on ferrihydrite, Co^{II} is oxidized to sorbed Co^{III} in agreement with the electron transfer to Fe^{III} atoms, which are reduced to Fe^{II} [95,97–101]. Simultaneously, both sorbed Co^{III} and free Co^{II} hydrolysis are responsible for H^+ generation, which facilitates local dissolution of ferrihydrite. Such phenomena are highlighted by conductivity fluctuations in the pH range 6 to 7.5. These latter numbers are in agreement with the progressive decrease in ferrihydrite crystallinity and particle size with increasing pH. The sequential adsorption–reprecipitation occurring on the ferrihydrite surface sites generate the $\text{Fe}^{\text{II}}/\text{Co}^{\text{III}}$ LDH nuclei clusters. Those positively charged nuclei attract anions. At pH 7, the association of nuclei and anions generate a pristine 3D organized $\text{Fe}^{\text{II}}/\text{Co}^{\text{III}}$ layered structure. Above pH 7, Co^{II} hydrolysis occurs. It is responsible for the local dissolution

of pristine LDHs, reprecipitation and then the 3D organization of $\text{Co}^{\text{II}}\text{Fe}^{\text{II}}\text{Co}^{\text{III}}_2$ LDHs, whose particle size and degree of crystalline organization increase along with the pH.

The progressive incorporation of Co^{II} into the LDH structure can account for two concomitant phenomena. The more Co^{II} is integrated into the LDHs, the greater the relative difference that evolves between the redox potentials, such as the redox couple $\text{Co}^{\text{III}}/\text{Co}^{\text{II}}$ becoming more oxidant than $\text{Fe}^{\text{III}}/\text{Fe}^{\text{II}}$. This shift allows the reverse redox reaction, such as Fe^{II} oxidizing to Fe^{III} , while Co^{III} reduces to Co^{II} within the LDH structure for the obtainment of $\text{Co}^{\text{II}}_6\text{Fe}^{\text{III}}_2$ LDHs. At the same time, the progressive incorporation of Co^{II} into the LDH structure is responsible for the decrease in the coulombic attraction between the positive surface layers and the interlayer anions and, thus, the progressive hydration of the material, which is, in turn, responsible for the progressive increase in the interlamellar space.

The nature of the interlamellar species (OH^- , HCO_3^- , CO_3^{2-} and NO_3^-) depends on the mobility and the speciation of anions with changing pH. Indeed, at pH 7, the LDH could be hydroxylated in agreement with the OH^- mobility $5.3 \times 10^{-9} \text{ m}\cdot\text{s}^{-1}$, which is nearly 3.0 and 4.5 times higher than that of NO_3^- and HCO_3^- , respectively. At pH 8 and 9, and at pH 11, HCO_3^- and then CO_3^{2-} are successively the predominant anions in the interlamellar space, in agreement with inorganic carbon speciation mechanisms.

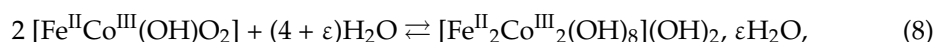
Following the insights that have been provided by these analyses, a mechanism for the formation of the LDHs Co/Fe is proposed and illustrated as follows (Equations (5) and (6)):



Ferrihydrite loses its protons (Equation (5)), and divalent cobalt is sorbed onto the negative-charged surface (Equation (6)). Then, Fe^{III} partly reduces to Fe^{II} , simultaneously with Co^{II} oxidizing to Co^{III} (Equation (7)).



Furthermore, x progressively increases until reaching 1, such as when $[\text{Fe}^{\text{III}}_{1-x}\text{Fe}^{\text{II}}_x(\text{OH})\text{O}_2] \cdot (\text{Co}^{\text{II}}_{1-x}\text{Co}^{\text{III}}_x)$ transforms to $[\text{Fe}^{\text{II}}\text{Co}^{\text{III}}(\text{OH})\text{O}_2]$, which reacts with H_2O , such as in Equation (8):

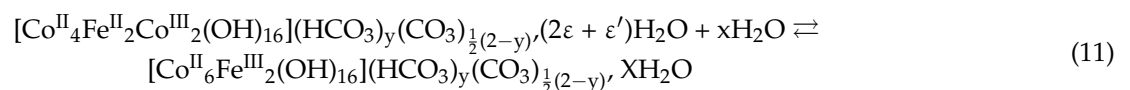
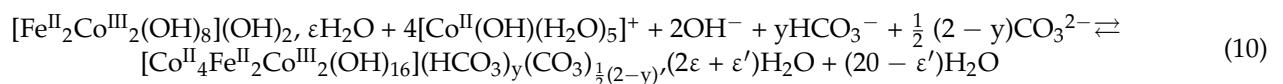


The obtainment of an $\text{Fe}^{\text{II}}/\text{Co}^{\text{III}}$ LDH is in agreement with the AAS and UV analyses, with OH^- anion predominant in the interlamellar space.

At the same time, Co^{II} in solution hydrolyzes as follows (Equation (9)):

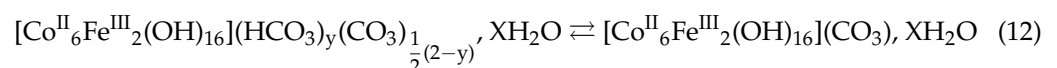


Such a phenomenon is responsible for local dissolution–reprecipitation and 3D organization, such as Co^{II} progressively integrating into the structure of the pristine LDHs, in agreement with Equations (10) and (11):



where $X = 2\varepsilon + \varepsilon' + x$, and Fe^{II} oxidizes while Co^{III} is reduced.

With the decrease in y with increasing pH, a solid is formed according to Equation (12):



The long-term storage of LDH particles as slurries at room temperature is responsible for the continuation of Ostwald maturation.

5. Conclusions

This study focused on the formation mechanisms of Co/Fe LDHs under high super-saturation conditions.

The monitoring of pH and conductivity carried out during titrations, together with PXRD characterization of solids, UV–visible characterization of dissolved solids and AAS analyses of the supernatants, allowed for the determination of the speciation of intermediates involved in the pathway to the formation of the final Co/Fe LDHs.

From pH 2, the pH increase induces Fe^{III} precipitation as ferrihydrite, which is the pristine reactional intermediate. The maintenance of such a structure in the pH range 3–6 is explained by Co^{II} and Na^I adsorption onto ferrihydrite. Co^{II} adsorption on ferrihydrite is responsible for modifying the relative position of the redox potential of Co^{III}/Co^{II} and Fe^{III}/Fe^{II} redox couples, such as when compared to pH, and Co^{II} becomes a reducing agent for Fe^{III} in ferrihydrite. Sorbed Co^{II} is thus oxidized to sorbed Co^{III} in agreement with the electron transfer to Fe^{III} atoms in the ferrihydrite structure, which are reduced to Fe^{II}. This phenomenon induces the decrease in ferrihydrite crystallinity. At the same time, at $6 \leq \text{pH} \leq 7$, both sorbed Co^{III} and free aqueous Co^{II} hydrolysis drive the amorphization of ferrihydrite, already in progress, into positively charged Fe^{II}/Co^{III} brucite-like nuclei, in agreement with dissolution–reprecipitation phenomena. At pH 7, these charged nuclei organize into a 3D Fe^{II}/Co^{III} LDH pristine structure, which is mainly hydroxylated. Above pH 7, Co^{II} hydrolysis proceeds and is responsible for the local dissolution of pristine LDHs and their reprecipitation and then 3D organization into Co^{II}₄Fe^{II}₂Co^{III}₂ LDHs. The progressive incorporation of cobalt into the LDH structure is responsible for the strength inversion of the redox potential of the two redox couples, Co^{III}/Co^{II} and Fe^{III}/Fe^{II}, such as when Fe^{II} (as a stronger reducing agent) re-oxidizes to Fe^{III} while Co^{III} (as a stronger oxidizing agent) is re-reduced to Co^{II}, for the obtainment of Co^{II}₆Fe^{III}₂ LDH. The long-term storage of LDH particles as slurries at room temperature is responsible for the continuation of Ostwald maturation. At pH 8 and 9, and at pH 11, HCO₃[−] and then CO₃^{2−} are successively the predominant anions in the interlamellar space, in agreement with inorganic carbon speciation mechanisms.

Supplementary Materials: The following supporting information can be downloaded at: <https://www.mdpi.com/article/10.3390/nano12091570/s1>; Figure S1. Modelled evolution of conductivity versus pH values during the modelled titration of dissolved Co(NO₃)₂ (0.15 M) and Fe(NO₃)₃ (0.05 M) by the alkaline titrant solution of NaOH (2.80 M) and Na₂CO₃ (0.78 M) at 35 °C, according to equilibria with ferrihydrite 2 line, ferrihydrite 6 line and Co(OH)₂; Figure S2. Evolution, versus time, of measured pH and Co²⁺ concentration provided by AAS and calculated using conductivity measurement; Figure S3. Rietveld refinement analyses of XRD patterns of solids synthesized at pH 7, 8, 9 and 11; Figure S4. Rietveld refinement analyses of XRD patterns of solids collected after ageing.

Author Contributions: Funding acquisition, S.B., A.S. and I.I.; Conceptualization, S.B. and A.S.; methodology, S.B. and A.S.; software, S.B. and N.M.; validation, S.B., A.S., N.M. and I.I.; formal analysis, C.M., S.B., N.M. and A.S.; investigation, C.M., S.B. and A.S.; data curation, S.B., C.M., N.M. and A.S.; writing—original draft preparation, C.M., S.B. and A.S.; writing—review and editing, S.B., A.S. and I.I. All authors have read and agreed to the published version of the manuscript.

Funding: This work was funded by ADEME (Agence de la Transition Ecologique–Ecological transition Agency) and the BRGM-LGC partnership (CALICE project 2018–2022).

Institutional Review Board Statement: Not applicable.

Informed Consent Statement: Not applicable.

Data Availability Statement: The data presented in this study are available within the article or supplementary material.

Acknowledgments: The authors thank ADEME and Aicha El Khamlichi for supporting the project, Cédric Duee for the SEM images, Abdeltif Lahfid for IRTF analyses and Kaoutar Eddarrajji for the UV–visible spectrophotometric measurements.

Conflicts of Interest: The authors declare no conflict of interest.

References

1. Rives, V. *Layered Double Hydroxides: Present and Future*; Nova Science Publishers: New York, NY, USA, 2001.
2. Othman, M.R.; Helwani, Z.; Martunus; Fernando, W.J.N. Synthetic hydrotalcites from different routes and their application as catalysts and gas adsorbents: A Review. *Appl. Organomet. Chem.* **2009**, *23*, 335–346. [[CrossRef](#)]
3. Nalawade, P.; Aware, B.; Kadam, V.J.; Hirlekar, R.S. Layered Double Hydroxides: A Review. *J. Sci. Ind. Res. (India)* **2009**, *68*, 267–272.
4. Duquesne, E.; Betelu, S.; Seron, A.; Ignatiadis, I.; Perrot, H.; Debiemme-Chouvy, C. Tuning redox state and ionic transfers of Mg/Fe-layered double hydroxide nanosheets by electrochemical and electrogravimetric methods. *Nanomaterials* **2020**, *10*, 1832. [[CrossRef](#)] [[PubMed](#)]
5. Bukhtiyarova, M.V. A review on effect of synthesis conditions on the formation of Layered Double Hydroxides. *J. Solid State Chem.* **2019**, *269*, 494–506. [[CrossRef](#)]
6. Lopez, T.; Bosch, P.; Ramos, E.; Gomez, R.; Novaro, O.; Acosta, D.; Figueras, F. Synthesis and characterization of sol-gel hydrotalcites. Structure and Texture. *Langmuir* **1996**, *12*, 189–192. [[CrossRef](#)]
7. Seron, A.; Delorme, F. Synthesis of Layered Double Hydroxides (LDHs) with varying pH: A valuable contribution to the study of Mg/Al LDH formation mechanism. *J. Phys. Chem. Solids* **2008**, *69*, 1088–1090. [[CrossRef](#)]
8. Tonelli, D.; Gualandi, I.; Musella, E.; Scavetta, E. Synthesis and characterization of Layered Double Hydroxides as materials for electrocatalytic applications. *Nanomater* **2021**, *11*, 725. [[CrossRef](#)]
9. Wang, Z.; Jia, W.; Jiang, M.; Chen, C.; Li, Y. Microwave-Assisted Synthesis of Layer-by-Layer Ultra-Large and Thin NiAl-LDH/RGO Nanocomposites and Their Excellent Performance as Electrodes. *Sci. China Mater.* **2015**, *58*, 944–952. [[CrossRef](#)]
10. Wang, J.; Ding, Q.; Bai, C.; Wang, F.; Sun, S.; Xu, Y.; Li, H. Synthesis of CNTS/CONIFE-LDH Nanocomposite with High specific surface area for asymmetric supercapacitor. *Nanomaterials* **2021**, *11*, 2155. [[CrossRef](#)]
11. Qiao, C.; Zhang, Y.; Zhu, Y.; Cao, C.; Bao, X.; Xu, J. One-Step Synthesis of Zinc-Cobalt Layered Double Hydroxide (Zn-Co-LDH) Nanosheets for High-Efficiency Oxygen Evolution Reaction. *J. Mater. Chem. A* **2015**, *3*, 6878–6883. [[CrossRef](#)]
12. Di Bitetto, A.; Kervern, G.; Andre, E.; Durand, P.; Carteret, C. Carbonate–hydrogenocarbonate coexistence and dynamics in Layered Double Hydroxides. *J. Phys. Chem. C* **2017**, *121*, 6104–6112. [[CrossRef](#)]
13. Aisawa, S.; Takahashi, S.; Ogasawara, W.; Umetsu, Y.; Narita, E. Direct intercalation of amino acids into Layered Double Hydroxides by coprecipitation. *J. Solid State Chem.* **2001**, *162*, 52–62. [[CrossRef](#)]
14. Theiss, F.L.; Ayoko, G.A.; Frost, R.L. Synthesis of Layered Double Hydroxides Containing Mg²⁺, Zn²⁺, Ca²⁺ and Al³⁺ Layer Cations by Co-Precipitation Methods—A Review. *Appl. Surf. Sci.* **2016**, *383*, 200–213. [[CrossRef](#)]
15. Tavares, S.R.; Haddad, J.F.S.; Ivo, R.; Moraes, P.; Leitão, A.A. Computational Exploration of the anion exchange on the basal surface of Layered Double Hydroxides by Molecular Dynamics. *Appl. Surf. Sci.* **2020**, *513*, 145743. [[CrossRef](#)]
16. Das, N.N.; Konar, J.; Mohanta, M.K.; Srivastava, S.C. Adsorption of Cr(VI) and Se(IV) from Their aqueous solutions onto Zr⁴⁺-substituted ZnAl/MgAl-Layered Double Hydroxides: Effect of Zr⁴⁺ Substitution in the Layer. *J. Colloid Interface Sci.* **2004**, *270*, 1–8. [[CrossRef](#)]
17. Agnel, M.I.; Grangeon, S.; Fauth, F.; Elkaim, E.; Claret, F.; Roulet, M.; Warmont, F.; Tournassat, C. Mechanistic and thermodynamic insights into anion exchange by green rust. *Environ. Sci. Technol.* **2020**, *54*, 851–861. [[CrossRef](#)]
18. Cavani, F.; Trifirò, F.; Vaccari, A. Hydrotalcite-Type Anionic Clays: Preparation, properties and applications. *Catal. Today* **1991**, *11*, 173–301. [[CrossRef](#)]
19. Santamaría, L.; Korili, S.A.; Gil, A. Layered Double Hydroxides from Slags: Closing the Loop. *Journal of Environmental Chemical Engineering. J. Environ. Chem. Eng.* **2022**, *10*, 106948. [[CrossRef](#)]
20. Karim, A.V.; Hassani, A.; Eghbali, P.; Nidheesh, P.V. Nanostructured Modified Layered Double Hydroxides (LDHs)-Based Catalysts: A Review on synthesis, characterization, and applications in water remediation by advanced oxidation processes. *Curr. Opin. Solid State Mater. Sci.* **2022**, *26*, 100965. [[CrossRef](#)]
21. Ye, H.; Liu, S.; Yu, D.; Zhou, X.; Qin, L.; Lai, C.; Qin, F.; Zhang, M.; Chen, W.; Chen, W.; et al. Regeneration Mechanism, modification strategy, and environment application of layered double hydroxides: Insights based on memory effect. *Coord. Chem. Rev.* **2022**, *450*, 214253. [[CrossRef](#)]
22. Mallakpour, S.; Hatami, M.; Hussain, C.M. Recent Innovations in Functionalized Layered Double Hydroxides: Fabrication, characterization, and industrial applications. *Adv. Colloid Interface Sci.* **2020**, *283*, 102216. [[CrossRef](#)]
23. Mendil, R.; Nasrallah, N. Zn-Fe Layered Double Hydroxides Synthesized by Three (03) Methods of Coprecipitation: Application to the removal of cochineal red dye from aqueous solution. *Fibers Polym.* **2021**, *22*, 3358–3367. [[CrossRef](#)]
24. Dewangan, N.; Hui, W.M.; Jayaprakash, S.; Bawah, A.R.; Poerjoto, A.J.; Jie, T.; Jangam, A.; Hidajat, K.; Kawi, S. Recent progress on layered double hydroxide (LDH) derived metal-based catalysts for CO₂ conversion to valuable chemicals. *Catal. Today* **2020**, *356*, 490–513. [[CrossRef](#)]

25. Mochane, M.J.; Magagula, S.I.; Sefadi, J.S.; Sadiku, E.R.; Mokhena, T.C. Morphology, Thermal Stability, and Flammability Properties of Polymer-Layered Double Hydroxide (LDH) Nanocomposites: A Review. *Crystals* **2020**, *10*, 612. [[CrossRef](#)]
26. Gu, Z.; Atherton, J.J.; Xu, Z.P. Hierarchical Layered Double Hydroxide Nanocomposites: Structure, synthesis and applications. *Chem. Commun.* **2015**, *51*, 3024–3036. [[CrossRef](#)] [[PubMed](#)]
27. Chatterjee, A.; Bharadiya, P.; Hansora, D. Layered Double Hydroxide Based bionanocomposites. *Appl. Clay Sci.* **2019**, *177*, 19–36. [[CrossRef](#)]
28. Wang, Q.; Tay, H.H.; Guo, Z.; Chen, L.; Liu, Y.; Chang, J.; Zhong, Z.; Luo, J.; Borgna, A. Morphology and Composition Controllable Synthesis of Mg–Al–CO₃ Hydrotalcites by Tuning the Synthesis pH and the CO₂ Capture Capacity. *Appl. Clay Sci.* **2012**, *55*, 18–26. [[CrossRef](#)]
29. Climent, M.J.; Corma, A.; Iborra, S.; Epping, K.; Vely, A. Increasing the basicity and catalytic activity of hydrotalcites by different synthesis procedures. *J. Catal.* **2004**, *225*, 316–326. [[CrossRef](#)]
30. Bocclair, J.W.; Braterman, P.S.; Jiang, J.; Lou, S.; Yarberr, F. Layered Double Hydroxide Stability. 2. Formation of Cr(III)-Containing Layered Double Hydroxides directly from solution. *Chem. Mater.* **1999**, *11*, 303–307. [[CrossRef](#)] [[PubMed](#)]
31. Bocclair, J.W.; Braterman, P.S. One-Step Formation and Characterization of Zn(II)-Cr(III) Layered Double Hydroxides, Zn₂Cr(OH)₆X (X = Cl, 1/2SO₄). *Chem. Mater.* **1998**, *10*, 2050–2052. [[CrossRef](#)] [[PubMed](#)]
32. Radha, A.V.; Kamath, P.V. Aging of Trivalent Metal Hydroxide/Oxide Gels in Divalent Metal Salt Solutions: Mechanism of formation of Layered Double Hydroxides (LDHs). *Bull. Mater. Sci.* **2003**, *26*, 661–666. [[CrossRef](#)]
33. Grégoire, B.; Ruby, C.; Carteret, C. Hydrolysis of Mixed Ni²⁺–Fe³⁺ and Mg²⁺–Fe³⁺ Solutions and mechanism of formation of Layered Double Hydroxides. *Dalt. Trans.* **2013**, *42*, 15687. [[CrossRef](#)]
34. Jolivet, J.-P.; Henry, M.; Livage, J. *De La Solution à l'oxyde: Condensation Des Cations En Solution Aqueuse, Chimie de Surface Des Oxydes*; InterEditions: Paris, France, 1994.
35. Zhao, J.; Chen, J.; Xu, S.; Shao, M.; Yan, D.; Wei, M.; Evans, D.G.; Duan, X. CoMn-Layered Double Hydroxide Nanowalls supported on carbon fibers for high-performance flexible energy storage devices. *J. Mater. Chem. A* **2013**, *1*, 8836–8843. [[CrossRef](#)]
36. Aristov, N.; Habekost, A. Cyclic Voltammetry—A Versatile electrochemical method investigating electron transfer processes. *World J. Chem. Educ.* **2015**, *3*, 115–119. [[CrossRef](#)]
37. Guoxiang, P.; Xinhui, X.; Jingshan, L.; Feng, C.; Zhihong, Y.; Hongjin, F. Preparation of CoAl Layered Double Hydroxide Nanoflake Arrays and Their High Supercapacitance Performance. *Appl. Clay Sci.* **2014**, *102*, 28–32. [[CrossRef](#)]
38. Loh, P.Y.; Lee, K.K.; Ng, Y.; Sow, C.H.; Chin, W.S. Co/Al Layered Double Hydroxides Nanostructures: A binderless electrode for electrochemical capacitor. *Electrochem. Commun.* **2014**, *43*, 9–12. [[CrossRef](#)]
39. Ma, K.Y.; Cheng, J.P.; Liu, F.; Zhang, X. Co-Fe Layered Double Hydroxides Nanosheets vertically grown on carbon fiber cloth for electrochemical capacitors. *J. Alloys Compd.* **2016**, *679*, 277–284. [[CrossRef](#)]
40. Li, H.; Gao, Y.; Wang, C.; Yang, G. A Simple electrochemical route to access amorphous mixed-metal hydroxides for supercapacitor electrode materials. *Adv. Energy Mater.* **2015**, *5*, 1401767. [[CrossRef](#)]
41. Wang, D.; Li, J.; Zhang, D.; Liu, T.; Zhang, N.; Chen, L.; Liu, X.; Ma, R.; Qiu, G. Layered Co–Mn Hydroxide nanoflakes grown on carbon cloth as binder-free flexible electrodes for supercapacitors. *J. Mater. Sci.* **2016**, *51*, 3784–3792. [[CrossRef](#)]
42. Chen, D.; Chen, H.; Chang, X.; Liu, P.; Zhao, Z.; Zhou, J.; Xu, G.; Lin, H.; Han, S. Hierarchical CoMn-Layered Double Hydroxide Nanowires on nickel foam as electrode material for high-capacitance supercapacitor. *J. Alloys Compd.* **2017**, *729*, 866–873. [[CrossRef](#)]
43. Patil, D.S.; Pawar, S.A.; Lee, S.H.; Shin, J.C. CoFe Layered Double Hydroxide for enhanced electrochemical performance. *J. Electroanal. Chem.* **2020**, *862*, 114012. [[CrossRef](#)]
44. Gupta, V.; Gupta, S.; Miura, N. Electrochemically Synthesized Large Area Network of Co_xNi_{1-x}Al_z Layered Triple Hydroxides Nanosheets: A High Performance supercapacitor. *J. Power Sources* **2009**, *189*, 1292–1295. [[CrossRef](#)]
45. Zhang, F.; Jiang, J.; Yuan, C.; Hao, L.; Shen, L.; Zhang, L.; Zhang, X. Glycine-Assisted Hydrothermal Synthesis of Nanostructured Co_xNi_{1-x}-Al Layered Triple Hydroxides as Electrode Materials for High-Performance Supercapacitors. *J. Solid State Electrochem.* **2012**, *16*, 1933–1940. [[CrossRef](#)]
46. Hu, M.; Ji, X.; Lei, L.; Lu, X. The effect of cobalt on the electrochemical performances of Ni-Al Layered Double Hydroxides used in Ni-M(H) battery. *J. Alloys Compd.* **2013**, *578*, 17–25. [[CrossRef](#)]
47. Duquesne, E.; Betelu, S.; Bazin, C.; Seron, A.; Ignatiadis, I.; Perrot, H.; Sel, O.; Debiemme-Chouvy, C. Insights into redox reactions and ionic transfers in Nickel/Iron Layered Double Hydroxide in Potassium Hydroxide. *J. Phys. Chem. B* **2020**, *124*, 3037–3049. [[CrossRef](#)]
48. Trotochaud, L.; Young, S.L.; Ranney, J.K.; Boettcher, S.W. Nickel-Iron oxyhydroxide oxygen-evolution electrocatalysts: The role of intentional and incidental iron incorporation. *J. Am. Chem. Soc.* **2014**, *136*, 6744–6753. [[CrossRef](#)]
49. Wang, K.; Zhang, L.; Su, Y.; Shao, D.; Zeng, S.; Wang, W. Photoreduction of carbon dioxide of atmospheric concentration to methane with water over CoAl-Layered Double Hydroxide Nanosheets. *J. Mater. Chem. A* **2018**, *6*, 8366–8373. [[CrossRef](#)]
50. Wulfsberg, G. *Principles of Descriptive Inorganic Chemistry*; University Science Books: South Orange, NJ, USA, 1991.
51. Su, L.H.; Zhang, X.G.; Mi, C.H.; Liu, Y. Insights into the electrochemistry of Layered Double Hydroxide Containing Cobalt and Aluminum elements in Lithium Hydroxide aqueous solution. *J. Power Sources* **2008**, *179*, 388–394. [[CrossRef](#)]
52. Scavetta, E.; Ballarin, B.; Berrettoni, M.; Carpani, I.; Giorgetti, M.; Tonelli, D. Electrochemical sensors based on electrodes modified with synthetic hydrotalcites. *Electrochim. Acta* **2006**, *51*, 2129–2134. [[CrossRef](#)]

53. Ballarin, B.; Seeber, R.; Tonelli, D.; Vaccari, A. Electrocatalytic properties of nickel^(II) hydrotalcite-type anionic clay: Application to methanol and ethanol Oxidation. *J. Electroanal. Chem.* **1999**, *463*, 123–127. [[CrossRef](#)]
54. Panda, H.S.; Srivastava, R.; Bahadur, D. Synthesis and in situ mechanism of nuclei growth of Layered Double Hydroxides. *Bull. Mater. Sci.* **2011**, *34*, 1599–1604. [[CrossRef](#)]
55. Yu, J.Y.; Park, M.; Kim, J. Solubilities of Synthetic schwertmannite and ferrihydrite. *Geochem. J.* **2002**, *36*, 119–132. [[CrossRef](#)]
56. Schwertmann, U. Solubility and dissolution of iron oxides. *Plant Soil* **1991**, *130*, 1–25. [[CrossRef](#)]
57. González, G.; Sagarzazu, A.; Villalba, R. Study of the Mechano-chemical transformation of goethite to hematite by TEM and XRD. *Mater. Res. Bull.* **2000**, *35*, 2295–2308. [[CrossRef](#)]
58. Cornell, R.M.; Schwertmann, U. *The Iron Oxides*; Wiley: Hoboken, NJ, USA, 2003. [[CrossRef](#)]
59. Das, S.; Hendry, M.J.; Essilfie-Dughan, J. Transformation of two-line ferrihydrite to goethite and hematite as a function of pH and temperature. *Environ. Sci. Technol.* **2011**, *45*, 268–275. [[CrossRef](#)]
60. Cudennec, Y.; Lecerf, A. The Transformation of ferrihydrite into goethite or hematite, revisited. *J. Solid State Chem.* **2006**, *179*, 716–722. [[CrossRef](#)]
61. Maillot, F.; Morin, G.; Wang, Y.; Bonnin, D.; Ildefonse, P.; Chaneac, C.; Calas, G. New Insight into the structure of nanocrystalline ferrihydrite: Exafs evidence for tetrahedrally coordinated Iron(III). *Geochim. Cosmochim. Acta* **2011**, *75*, 2708–2720. [[CrossRef](#)]
62. Janney, D.E.; Crowley, J.M.; Buseck, P.R. Structure of synthetic 6-Line ferrihydrite by electron nanodiffraction. *Am. Mineral.* **2001**, *86*, 327–335. [[CrossRef](#)]
63. Michel, F.M.; Ehm, L.; Liu, G.; Han, W.Q.; Antao, S.M.; Chupas, P.J.; Lee, P.L.; Knorr, K.; Eulert, H.; Kim, J.; et al. Similarities in 2- and 6-line ferrihydrite based on pair distribution function analysis of x-ray total scattering. *Chem. Mater.* **2007**, *19*, 1489–1496. [[CrossRef](#)]
64. Jambor, J.L.; Dutrizac, J.E. Occurrence and Constitution of natural and synthetic ferrihydrite, a widespread iron oxyhydroxide. *Chem. Rev.* **1998**, *98*, 2549–2585. [[CrossRef](#)]
65. Drits, V.A.; Sakharov, B.A.; Salyn, A.L.; Manceau, A. Structural model for ferrihydrite. *Clay Miner.* **1993**, *28*, 185–207. [[CrossRef](#)]
66. Su, L.W. Cobalt Adsorption and/or Co-Precipitation onto Ferric Oxyhydroxide. Ph.D. Thesis, University of British Columbia, Vancouver, BC, Canada, 2011. [[CrossRef](#)]
67. Fei, Y.; Hua, J.; Liu, C.; Li, F.; Zhu, Z.; Xiao, T.; Chen, M.; Gao, T.; Wei, Z.; Hao, L. Aqueous Fe(II)-Induced Phase transformation of ferrihydrite coupled adsorption/immobilization of rare earth elements. *Minerals* **2018**, *8*, 357. [[CrossRef](#)]
68. Adra, A. Structure et Réactivité des Nano-Oxyhydroxydes de fer et D'aluminium en aval D'un drainage Minier Acide. Ph.D. Thesis, Université Paris, Paris, France, 2014.
69. Liu, C.; Zhu, Z.; Li, F.; Liu, T.; Liao, C.; Lee, J.J.; Shih, K.; Tao, L.; Wu, Y. Fe(II)-Induced Phase transformation of ferrihydrite: The Inhibition effects and stabilization of divalent metal cations. *Chem. Geol.* **2016**, *444*, 110–119. [[CrossRef](#)]
70. Riley, E.; Dutrizac, J.E. The Behaviour of the rare earth elements during the precipitation of ferrihydrite from sulphate media. *Hydrometallurgy* **2017**, *172*, 69–78. [[CrossRef](#)]
71. Masue-Slowey, Y.; Loepfert, R.H.; Fendorf, S. Alteration of ferrihydrite reductive dissolution and transformation by adsorbed As and structural Al: Implications for As retention. *Geochim. Cosmochim. Acta* **2011**, *75*, 870–886. [[CrossRef](#)]
72. Massey, M.S.; Lezama-Pacheco, J.S.; Michel, F.M.; Fendorf, S. Uranium incorporation into Aluminum-substituted ferrihydrite during Iron(II)-induced transformation. *Environ. Sci. Process. Impacts* **2014**, *16*, 2137–2144. [[CrossRef](#)]
73. Malherbe, F.; Bigey, L.; Forano, C.; De Roy, A.; Besse, J.P. Structural aspects and thermal properties of Takovite-like Layered Double Hydroxides pillared with chromium oxo-anions. *J. Chem. Soc. Dalton Trans.* **1999**, *21*, 3831–3839. [[CrossRef](#)]
74. Evans, D.G.; Slade, R.C.T. Structural aspects of Layered Double Hydroxides. *Struct. Bond.* **2005**, *119*, 1–87. [[CrossRef](#)]
75. Ma, K.; Cheng, J.P.P.; Zhang, J.; Li, M.; Liu, F.; Zhang, X. Dependence of Co/Fe ratios in Co-Fe Layered Double Hydroxides on the structure and capacitive properties. *Electrochim. Acta* **2016**, *198*, 231–240. [[CrossRef](#)]
76. Tamaki, T.; Nakanishi, N.; Ohashi, H.; Yamaguchi, T. The Effect of Particle Size and surface area on the ion conductivity of Layered Double Hydroxide. *Electrochem. Commun.* **2012**, *25*, 50–53. [[CrossRef](#)]
77. Wang, Q.; O'Hare, D. Recent advances in the synthesis and application of Layered Double Hydroxide (LDH) Nanosheets. *Chem. Rev.* **2012**, *112*, 4124–4155. [[CrossRef](#)] [[PubMed](#)]
78. Hur, T.-B.; Phuoc, T.X.; Chyu, M.K. New approach to the synthesis of Layered Double Hydroxides and associated ultrathin nanosheets in de-ionized water by laser ablation. *J. Appl. Phys.* **2010**, *108*, 114312. [[CrossRef](#)]
79. Song, F.; Hu, X. Exfoliation of Layered Double Hydroxides for enhanced oxygen evolution catalysis. *Nat. Commun.* **2014**, *5*, 4477. [[CrossRef](#)] [[PubMed](#)]
80. Kim, S.J.; Lee, Y.; Lee, D.K.; Lee, J.W.; Kang, J.K. Efficient Co-Fe Layered Double hydroxide photocatalysts for water oxidation under visible light. *J. Mater. Chem. A* **2014**, *2*, 4136–4139. [[CrossRef](#)]
81. Nejati, K.; Zabihi, R. Preparation and magnetic properties of nano size nickel ferrite particles using hydrothermal method. *Chem. Cent. J.* **2012**, *6*, 1–6. [[CrossRef](#)]
82. Zhang, F.; Yuan, C.; Lu, X.; Zhang, L.; Che, Q.; Zhang, X. Facile growth of mesoporous co 3o 4 nanowire arrays on ni foam for high performance electrochemical capacitors. *J. Power Sources* **2012**, *203*, 250–256. [[CrossRef](#)]
83. Iyi, N.; Fujii, K.; Okamoto, K.; Sasaki, T. Factors Influencing the Hydration of Layered Double Hydroxides (LDHs) and the Appearance of an Intermediate Second Staging Phase. *Appl. Clay Sci.* **2007**, *35*, 218–227. [[CrossRef](#)]

84. Guan, H.; Shao, C.; Wen, S.; Chen, B.; Gong, J.; Yang, X. A Novel method for preparing Co_3O_4 nanofibers by using electrospun pva/cobalt acetate composite fibers as precursor. *Mater. Chem. Phys.* **2003**, *82*, 1002–1006. [[CrossRef](#)]
85. Allen, G.C.; Paul, M. Chemical Characterization of Transition Metal Spinel-Type Oxides by Infrared Spectroscopy. *Appl. Spectrosc.* **1995**, *49*, 451–458. [[CrossRef](#)]
86. Lin, M.C.; Chang, F.T.; Uan, J.Y. Synthesis of Li-Al-Carbonate Layered Double Hydroxide in a Metal Salt-Free System. *J. Mater. Chem.* **2010**, *20*, 6524–6530. [[CrossRef](#)]
87. Miller, F.A.; Wilkins, C.H. Infrared Spectra and Characteristic Frequencies of Inorganic Ions. *Anal. Chem.* **1952**, *24*, 1253–1294. [[CrossRef](#)]
88. Gregoire, B. Relation Composition Structure des Hydroxydes Doubles Lamellaires: Effets de la Charge du Feuillet et de la Nature de L'anion Interfoliaire. Ph.D. Thesis, Université de Lorraine, Nancy, France, 2012.
89. Gregoire, B.; Andre, E.; Ruby, C.; Carteret, C. Tuning and Investigating the structure of MII-FeIII Layered Double Hydroxides (MII = NiII, CoII and MgII) in relation to their composition: From synthesis to anionic exchange properties. *Curr. Inorg. Chem.* **2015**, *5*, 169–183. [[CrossRef](#)]
90. Etique, M.; Zegeye, A.; Grégoire, B.; Carteret, C.; Ruby, C. Nitrate Reduction by Mixed Iron(II-III) Hydroxycarbonate green rust in the presence of phosphate anions: The key parameters influencing the ammonium selectivity. *Water Res.* **2014**, *62*, 29–39. [[CrossRef](#)]
91. Wang, L.; Zhang, Y.; Park, Y.; Chen, L.; Jung, Y.M. Quantitative Determination of Iron Ions Based on a Resonance Raman (RR) Probe-Phenanthroline. *Anal. Sci.* **2017**, *33*, 23–27. [[CrossRef](#)]
92. Majzlan, J.; Navrotsky, A.; Schwertmann, U. Thermodynamics of Iron Oxides: Part III. Enthalpies of formation and stability of Ferrihydrite ($\sim\text{Fe}(\text{OH})_3$), Schwertmannite ($\sim\text{FeO}(\text{OH})_{3/4}(\text{SO}_4)_{1/8}$), and $\epsilon\text{-Fe}_2\text{O}_3$. *Geochim. Cosmochim. Acta* **2004**, *68*, 1049–1059. [[CrossRef](#)]
93. Caron, M.H. Fundamental and practical factors in ammonia leaching of Nickel and Cobalt ores. *JOM* **1950**, *2*, 67–90. [[CrossRef](#)]
94. Osseo-Asare, K.; Fuerstenau, D.W. Adsorption phenomena in hydrometallurgy, 1 The Uptake of copper, nickel and cobalt by oxide adsorbents in aqueous ammoniacal solutions. *Int. J. Miner. Process.* **1979**, *6*, 85–104. [[CrossRef](#)]
95. Zhang, S.; Li, H.; Wu, Z.; Post, J.E.; Lanson, B.; Elzinga, E.J.; Liu, Y.; Li, H.; Hong, M.; Liu, F.; et al. Effects of Co Doping on the structure and physicochemical properties of hausmannite (Mn_3O_4) and its transformation during aging. *Chem. Geol.* **2021**, *582*, 120448. [[CrossRef](#)]
96. Yin, H.; Sun, J.; Yan, X.; Yang, X.; Feng, X.; Tan, W.; Qiu, G.; Zhang, J.; Ginder-Vogel, M.; Liu, F. Effects of Co^{II} ion exchange, Ni(II)- and V(V)-doping on the transformation behaviors of Cr(III) on hexagonal turbostratic birnessite-water interfaces. *Environ. Pollut.* **2020**, *256*, 113462. [[CrossRef](#)]
97. Boland, D.D.; Collins, R.N.; Glover, C.J.; David Waite, T. An In Situ Quick-EXAFS and Redox Potential Study of the Fe^{II} -Catalysed Transformation of Ferrihydrite. *Colloids Surf. A Physicochem. Eng. Asp.* **2013**, *435*, 2–8. [[CrossRef](#)]
98. Lan, S.; Wang, X.; Xiang, Q.; Yin, H.; Tan, W.; Qiu, G.; Liu, F.; Zhang, J.; Feng, X. Mechanisms of Mn(II) Catalytic oxidation on ferrihydrite surfaces and the formation of manganese (oxyhydr)oxides. *Geochim. Cosmochim. Acta* **2017**, *211*, 79–96. [[CrossRef](#)]
99. Alvarez, M.; Sileo, E.E.; Rueda, E.H. Structure and reactivity of synthetic Co-substituted goethites. *Am. Mineral.* **2008**, *93*, 584–590. [[CrossRef](#)]
100. Yin, H.; Wu, Y.; Hou, J.; Yan, X.; Li, Z.; Zhu, C.; Zhang, J.; Feng, X.; Tan, W.; Liu, F. Preference of Co over Al for substitution of Fe in goethite ($\alpha\text{-FeOOH}$) structure: Mechanism revealed from EXAFS, XPS, DFT and Linear free energy correlation model. *Chem. Geol.* **2020**, *532*, 119378. [[CrossRef](#)]
101. Bordeneuve, H.; Tenaillon, C.; Guillemet-Fritsch, S.; Smith, R.; Suard, E.; Rousset, A. Structural variations and cation distributions in $\text{Mn}_{3-x}\text{Co}_x\text{O}_4$ ($0 \leq x \leq 3$) dense ceramics using neutron diffraction data. *Solid State Sci.* **2010**, *12*, 379–386. [[CrossRef](#)]